Atmos. Chem. Phys. Discuss., 10, 14241–14312, 2010
www.atmos-chem-phys-discuss.net/10/14241/2010/
doi:10.5194/acpd-10-14241-2010

Atmospheric Chemistry and Physics Discussions

Mass tracking for chemical analysis: the causes of ozone formation in southern Ontario during BAQS-Met 2007

P. A. Makar[1], J. Zhang[1], W. Gong[1], C. Stroud[1], D. Sills[2], K. L. Hayden[1], J. Brook[1], I. Levy[1], C. Mihele[1], M. D. Moran[1], D. W. Tarasick[1], and H. He[1]

[1]Air Quality Research Division, Science and Technology Branch, Environment Canada, 4905 Dufferin Street, Toronto, Ontario, Canada
[2]National Laboratory for Nowcasting and Remote Sensing Meteorology, Environment Canada, 4905 Dufferin Street, Toronto, Ontario, Canada

Received: 28 April 2010 – Accepted: 26 May 2010 – Published: 9 June 2010

Correspondence to: P. A. Makar (paul.makar@ec.gc.ca)

Published by Copernicus Publications on behalf of the European Geosciences Union.

Abstract

A three-level nested regional air pollution model has been used to study the processes leading to high ozone concentrations in the southern Great Lakes region of North America. The highest resolution simulations show that complex interactions between the lake breeze circulation and the synoptic flow lead to significant enhancements in the photochemical production and transport of ozone at the local scale. Significant improvements in model correlation with ozone observations are achieved in going to the highest spatial resolution. Mass tracking of individual model processes show that Lakes Erie and St. Clair frequently act as photochemical production regions, with average mid-day production rates of 6 to 8 ppbv per hour. Enhanced ozone levels are evident over these two lakes in 23-day-average surface ozone fields. Analysis of other model fields and aircraft measurements suggests that vertical recirculation enhances ozone levels over Lake St. Clair while strong subsidence enhances ozone over Lake Erie. The mass tracking of model transport shows that lake-breeze surface convergence zones combined with the synoptic flow can carry ozone and its precursors hundreds of kilometers from these source areas, in narrow, elongated features. Comparison with surface mesonet ozone observations confirm the presence, magnitude, and timing of these features, which create local ozone enhancements on the order of 20 ppbv above the regional ozone levels. High-resolution modelling is recommended in order to predict these local-scale features in operational air-quality forecasts.

1 Introduction

The local and mesoscale circulations that arise from contrasts in the heat capacity of land versus water can have a significant effect on air pollution. For large bodies of water (oceans, large lakes), a diurnally varying circulation frequently develops during the warm season. Air over the land is warmed after sunrise while the air over the water is warmed much less, resulting in local pressure differences. These pressure

ACPD
10, 14241–14312, 2010

differences drive a local circulation, with air descending over the water and rising over the land during the day, with the reverse occurring at night. This in turn induces daytime divergence at the surface over the water, surface convergence over the land, with a return circulation aloft. The daytime surface divergence and associated water-to-land wind flow is known as the lake- or sea-breeze, while the reverse circulation is referred to as the land breeze (cf. Stull, 1988). The leading edge of the intrusion of marine air onto land may sometimes create a sharp gradient in temperature, wind speed, relative humidity and atmospheric stability; a lake (or sea) breeze front. Air-lake temperature contrasts less than 12 °C are sufficient to induce this circulation (Laird et al., 2001). In light winds, temperature constrasts of only a few degrees are sufficient to induce the circulation – as synoptic wind speeds increase, larger contrasts are required.

Non-reactive tracer modelling studies of coastal Los Angeles noted the ability of sea-breeze-induced fronts (sometimes coupled with topographic effects) to provide sufficient vertical transport to loft pollutants to high levels during the day, in turn creating layers of high concentration pollutants with the onset of more stable conditions at night (Lu and Turco, 1995). This finding has also been found in numerous measurement studies in coastal environments (cf. Li, 2004). The sea or lake breeze is often weak with respect to the synoptic flow, but combinations of the two have frequently been shown to give rise to elevated pollution levels. Example locations include Taiwan in the autumn (Cheng, 2002), Houston (Banta et al., 2005), Vancouver (Li, 2004), Marseille (Mestayer et al., 2005; Lasry et al., 2005) , Madrid and Valencia (Millán et al., 1997; Millán et al., 2000).

Houston is sometimes severely affected by sea-breeze-enhanced ozone levels. Analyses of surface winds, upper level synoptic maps and meteorological conditions have showed that the highest ozone days in that city are associated with the passage of sea-breeze fronts (Darby, 2005; Rappenglück et al., 2008). Cluster analysis of surface winds showed that these events correspond to the situation wherein transition from offshore to onshore flow is separated by a period of stagnation greater than or equal to one hour, up to six hours before the ozone event (Darby, 2005). The timing of the arrival

ACPD
10, 14241–14312, 2010

of the sea-breeze front is the key factor in predicting high pollution events in Houston, and sea-breezes in opposition to the synoptic flow lead to the highest pollution, due to recirculation of processed air (Banta et al., 2005). The depth of penetration of sea-breeze fronts onto land is dependant on the direction of the synoptic wind, as well as on the local radiative balance and land surface characteristics; (Cheng and Byun, 2008), and these factors in turn have a more significant effect on ozone forecasts than, for example, the choice of plume rise parameterization in an air-quality model (Cheng et al., 2008). The placement of major emissions sources relative to regularly repeating sea-breeze locations also has a significant impact on both ozone formation and dilution in the Greater Houston area (Byun et al., 2007).

The city of Marseille has been another focus for sea-breeze induced meteorological and air pollution studies. High resolution modelling studies have suggested that sea- and lake-breezes interact with Marseille's VOC emissions to create high ozone episodes (Lasry et al., 2005). Sophisticated urban heat island modelling for the same region suggests that Marseille's urban heat island circulation is affected by the sea-breeze: the urban circulation when the city was affected by sea-breezes was suppressed relative to instances of synoptic flows originating over the land (Lemonsu et al., 2006a; Drobinski et al., 2007). Work by the same group (Lemonsu et al., 2006b) suggested the presence of "deep" and "shallow" sea-breeze circulations, the former inhibited by topography, the latter enhanced by topography. Relatively low NO_2 and high O_3 in the Marseille marine boundary layer (indicative of a more photochemically aged airmass) suggest that it is an efficient photochemical reactor (Puygrenier et al., 2005). Pollutant concentrations in Marseille maximize just upwind of the sea-breeze front (the front propagation speed is lower than the wind speed, and the vertical mass flux at the front is less than the horizontal flux within the sea-breeze, allowing pollutants to accumulate just behind the front, with some upward transport; (Drobinski et al., 2007). The accurate simulation of the fine-scale features of sea-breeze mesoscale transport in the Marseille area is crucial in order to predict both ozone peaks and ozone plumes (Pirovano et al., 2007).

ACPD
10, 14241–14312, 2010

The surface temperature during the passage of Marseille's sea-breeze front has been found to be oscillatory (Puygrenier et al., 2005; Drobinski et al., 2007). Cold air transported inland due to sea-breezes results in temporarily increased stability over the land (isentrope inclination allows the sea-breeze flow to run along the slope, and adiabatic cooling associated with rising air retards the flow). The stability is short-lived, as solar energy is transferred to the surface, triggering turbulent vertical transport including convection. The upward motion results in surface level convergence over the land – this in turn amplifies the sea-breeze flow, which in turn advects cooler air over the land, increasing stability again, and slowing forward motion until the cycle repeats. Recent attempts to model this observed oscillatory flow have been unsuccessful (Drobinski et al., 2007).

The two main mechanisms for venting of Marseille's boundary layer air to the free troposphere are upslope winds enhanced by sea breezes, and frontogenesis at the sea-breeze front, with associated turbulence and upward motion (Bastin and Drobinksi, 2006). This venting is of sufficient magnitude to prevent significant recirculation of aged air back into the PBL (Drobinski et al., 2007).

Recirculation of aged polluted air in sea-breeze fronts has been observed elsewhere, however. Along the New England coastline, recirculation of aged air in sea-breeze fronts has been observed to increase ozone concentrations by 10 to 30 ppbv (Darby et al., 2007). The same study showed the presence of ozone aloft available for downward transport in frontal circulation along with recirculation patterns along the coast, but the observational evidence was not always sufficient to determine the cause of high ozone events (e.g. three possible sources for an event on 4 August 2004). Recirculation also has a significant impact on pollutants along the eastern Mediterranean (Levy et al., 2008). As in the Marseille studies, the interaction between synoptic and mesoscale flow was found to govern the impact of the sea breeze on air pollution. The location of urban heat islands and the shape of the coastline modified the sea-breeze, with the former reducing sea-breeze intensity, and the latter creating convergence regions which intensified it. The mechanism for sea-breeze impacts on eastern Mediterranean

ACPD
10, 14241–14312, 2010

ozone levels is unclear, with high ozone levels occurring for both high and low recirculation, and an anti-correlation with NO_x, suggesting both local and long-range transport sources of ozone.

Observational studies of lake-breeze fronts and their impacts on air pollution in the region of the Great Lakes of North America began in the 1960's (Mukammal, 1965; Lyons and Cole 1973, 1976; Lyons and Olsson, 1973; Anlauf et al., 1975). Model simulations of the air pollution associated with lake breeze circulation started with simple Gaussian dispersion models of non-reactive tracers, but the limitations of these models (Lyons et al., 1983) led to the use of full mesoscale models at resolutions of 1 to 10 km as the drivers for non-reactive tracer dispersion studies (Lyons et al., 1995). The lake-breeze circulation was found to be considerably more complex than previously expected; simulated non-reactive tracer plumes released at the shoreline were entirely transported out of the shallow lake-breeze inflow layer upon reaching the lake-breeze front. Plumes followed helical and even bifurcating trajectories (Lyons et al., 1995).

The reactive ozone chemistry associated with lake-breeze fronts in southern Ontario was first examined in the 1980's and 1990's. Some of this early work (e.g., Yap et al., 1988) suggested that local impacts on ozone levels were generally small, while some noted a more significant impact (Mukammal et al., 1982, 1985). Ozone concentration increases of 30 ppbv over the course of a few minutes were linked through surface station and satellite observations to the passage of a lake-breeze front in a later, more detailed analysis (Hastie et al., 1999). Time-coincident aircraft measurements of precursor NO_x and VOCs suggested that the airmass associated with the ozone maxima was well-aged, and moved inland from a position originating over Lake Ontario.

A common factor of the work to date on lake- or sea-breeze fronts is their complex nature; they are very local-scale features which nevertheless may have a profound impact on surface ozone concentrations in polluted regions. Three-dimensional mesoscale meteorological and air-quality models have provided a useful means of analyzing that complexity in Los Angeles, Houston, Taiwan and Marseille. In the study which follows, we use nested meteorological and pollution models to analyze ozone

ACPD
10, 14241–14312, 2010

formation in lake-breeze fronts in southern Ontario. As part of that analysis, we use the concept of mass- or operator-tracking, in which the changes to a pollutant's concentration (in this case, ozone) are tracked through every operator of the air-quality model, allowing us to quantitatively state the relative importance of different processes towards ozone formation in the study region.

The Border Air-Quality Study and Meteorology Study (BAQS-Met) was conducted in the region between Lakes Huron, St. Clair, and Erie, with the aim of studying the impact of lake breezes on local air-quality and long-range-transported chemistry. The study comprised a measurement-intensive field campaign from 20 June to 10 July 2007, as well as a local monitoring network that operated from the months of June through August. A variety of measurements for particulate matter and gases were carried out at three supersites (Bear Creek, Harrow and Ridgetown), on board the National Research Council of Canada (NRC) Twin Otter aircraft, and on Environment Canada's CRUISER mobile laboratory as part of the study. A ten-site mesonet monitoring network for 5-min average ozone and $PM_{2.5}$ was installed in the study region, in addition to ozone and $PM_{2.5}$ observations available from larger scale monitoring networks (AIRNow).

The work that follows has two main components. First, following a discussion on our methodology (Sect. 2), we present a formal statistical evaluation of the model using the available data (Sect. 3). Second, we make use of the model output to infer the physical and chemical causes for ozone formation in the region, using time sequences of model concentration fields, process mass tracking, and comparison of model and observed ozone time series (Sect. 4). The implications of the analysis and concluding remarks are presented in Sect. 5.

ACPD
10, 14241–14312, 2010

2 Methodology

2.1 Modelling system description

AURAMS (A Unified Regional Air-quality Modelling System) consists of three main components: (a) a prognostic meteorological model, GEM (Global Environmental Multiscale model: Côté et al., 1998); (b) an emissions processing system, SMOKE (Sparse Matrix Operator Kernel Emissions: Houyoux et al., 2000; CEP, 2003) ; and (c) an offline regional chemical transport model, the AURAMS Chemical Transport Model (CTM: cf. Cho et al., 2009; Gong et al., 2006; Makar et al.; 2009; Smyth et al., 2009; Stroud et al., 2008).

The GEM meteorological model is an integrated weather forecasting and data assimilation system that was designed to meet Canada's operational needs for both short- and medium-range weather forecasts. For the BAQS-Met simulations, GEM version 3.2.2 with physics version 4.5 was run on two domains: a variable-resolution global horizontal grid with a core domain covering North America (575×641 grid points over the globe, with 432×565 grid points over North America, 0.1375° or approximately 15.3-km grid spacing in the core region, 450-s timestep), and a local domain covering the Great Lakes area (565×494 grid points, 0.0225° or approximately 2.5-km grid spacing, 60-s timestep). The coarse-grid output was used to provide boundary conditions for the high-resolution domain meteorological simulations (Fig. 1), and the coarse resolution domain was driven by the operational objective analysis. The model employs 58 hybrid-coordinate levels from the Earth's surface to 10 hPa, with layer thickness increasing monotonically with height. The standard version of GEM 3.2.2 was modified to include a parameterization for urban heating (Makar et al., 2006). Additional improvements included a temperature-gradient-based boundary layer height parameterization, and consistency improvements for the model-generated vertical diffusion coefficients in the lowest model layers.

The multi-pollutant, regional AURAMS CTM was developed as a tool to study the formation of ozone, PM, and acid deposition in a single "unified" framework. The PM size

ACPD
10, 14241–14312, 2010

distribution in this study was represented using 12 size bins ranging from 0.01 to 41 µm in Stokes diameter and nine chemical components: sulphate (p-SO_4); nitrate (p-NO_3); ammonium (p-NH_4); elemental carbon (EC); primary organic matter (POM); secondary organic matter (SOM); crustal material (CM); sea salt; and particle-bound water. PM is assumed to be internally mixed in each size bin. Process representations in version 1.4.0 of the AURAMS CTM include emissions from surface and from elevated sources, horizontal and vertical advection, vertical diffusion, gas-phase, aqueous-phase, and inorganic heterogeneous chemistry, secondary organic particle formation, dry and wet deposition, and particle nucleation, condensation, coagulation, sedimentation, and activation (Gong et al., 2006).

A three level internal nesting setup was used for the AURAMS v1.4.0 simulations: 42-km/15-min North American domain, in turn driving a 15-km/15-min Eastern North American domain, in turn driving a 2.5-km/2-min Southern Ontario domain (Fig. 2). All model resolutions make use of a time-invariant upper boundary condition for the chemical species, and the outermost domain also makes use of time-invariant and vertically-varying chemical lateral boundary conditions (Makar et al., 2009). Twenty-eight terrain-following vertical levels stretched telescopically from the Earth's surface to 29 km, with the first three levels at 0, 13.9, and 55 m a.g.l. Up to 157 model species (gases and chemically speciated particle size bins) may be selected as model output, although gaseous species, primarily ozone, will be the focus in the current work.

Files of gridded hourly emission fields for input by the AURAMS CTM were prepared using version 2.2 of the SMOKE emissions processing system for four major emissions streams: on-road mobile sources; area and offroad-mobile sources, minor point sources; and major point sources. Emitted (i.e., "primary") PM from these sources is speciated within the AURAMS CTM based on speciation profiles for each emissions stream. The base year for the anthropogenic emissions was 2005 for the USA and for Canada, and 1999 for Mexico. Biogenic emissions are calculated using BEIS3.09 algorithms, with model generated temperatures and photosynthetically active radiation being used to create these emissions during the model runs.

ACPD
10, 14241–14312, 2010

2.2 Simulation period and operating sequence

Both GEM and the AURAMS CTM were run for the 3-month period from 1 June 2007 to 31 August 2007, for the GEM 15-km and AURAMS 42-km and 15-km domains. The GEM 15-km meteorology was used to drive the AURAMS CTM at both 42 and 15 km. The GEM 15-km meteorology was also used for boundary conditions for the higher resolution GEM 2.5-km simulation, in turn used to drive the higher resolution AURAMS simulation. The GEM 2.5-km and AURAMS 2.5-km simulations were only run for dates encompassing the BAQS-Met measurement intensive (17 June to 11 July 2007). The lateral boundary conditions for the 15-km and 2.5-km AURAMS CTM simulations were taken from the corresponding coarser resolution simulations in each case; the climatological boundary condition was used for the model top in all three AURAMS simulations.

The GEM meteorology was created in a sequence of 12 h runs, starting at 0, 6, 12 and 18 Z from objective analysis files at those times for the 15-km simulation, the first six hours of these simulations being used for model spin-up, the last six hours being retained for AURAMS simulations. This methodology makes use of the meteorological data assimilation of the objective analysis to the maximum extent, to prevent chaotic drift of the predicted 15-km meteorology from the observations. The 2.5-km GEM simulation made use of the 15-km GEM simulation as boundary conditions.

2.3 Model diagnostics: extraction of model values and mass tracking

2.3.1 Extraction of model values

Times series of surface ozone at hourly intervals were extracted from the 42-km and 15-km AURAMS simulations for comparison to AIRNow observations. Time series of surface ozone concentrations were extracted on the two minute AURAMS 2.5-km domain time-step at each of the fixed station sites of the BAQS-Met intensive. The mesonet ozone site 5-min averages were summed to create hourly averages, and the

ACPD
10, 14241–14312, 2010

corresponding AURAMS 2.5-km/2-min output values were summed to create equivalent hourly averages for statistical analysis. Aircraft ozone observations (Hayden et al., 2010) were five second resolution data: these were binned to two minutes for comparison to AURAMS' output. The speed of the aircraft was sufficiently high to traverse several model gridpoints in a two minute interval. In order to more closely match the model to measurement locations, the aircraft locations at 10 second intervals during each two minute model step were used to extract the model values along the same 3-D flight path in the model coordinate system. The average of the ten second values interpolated from the model grid, during that 2 min interval, along that flight path, was used to create the corresponding "model" value for statistical comparison to the aircraft data. The ozone measurements from the mobile laboratory CRUISER were one minute averages: the speed of the mobile laboratory is sufficiently slow that the nearest model gridpoint to the CRUISER location is sufficiently accurate for comparison purposes.

2.3.2 Mass tracking of ozone

As is the case for most regional transport models, AURAMS makes use of operator splitting (Marchuk, 1975) for the numerical solution of the system of differential equations describing the rate of change of the chemical constituents in the atmosphere: the different components (operators) of the net equation are solved in sequence, with the solution from each operator in the sequence becoming the initial concentrations for the next operator in the sequence. Each component operates over the net time step of the model. AURAMS v1.4.0 includes an analysis package that records the change in mass of selected model species through each of the model operators. The change in mass for each component of the model atmosphere across each of these operators may be tracked in AURAMS; the mass prior to the operator is subtracted from the mass subsequent to the operator, in order to determine the net change in mass for that operator for that time step (which is then expressed in units of ppbv/hour). These mass tracking options allow comparison of the gas-phase chemical production and loss, the advection, and the diffusion and deposition operators for ozone, within the AURAMS

ACPD
10, 14241–14312, 2010

simulations. The relative magnitude and sign of the operators thus give information regarding the reasons for the model's ozone predictions, hence providing hypotheses for ozone formation, destruction, and transport, in the ambient atmosphere. This concept has appeared elsewhere in the literature, as *process analysis* (cf. Gipson, 1999; Jang et al, 1995; Jeffries and Tonnesen, 1994).

3 Model performance evaluation

3.1 AURAMS 42-km and 15-km ozone versus AIRNow observations

Hourly ozone measurements from the near-real-time AIRNow metanetwork were compared to the 42-km and 15-km AURAMS output for the period 3 June 2007 through 31 August 2007, with the results depicted in Table 1. Evaluation statistics are computed for each AIRNow site (nearest neighbour grid-cell from the model) with regard to hourly ozone values, daily 1-h average ozone maxima, and daily mean ozone values. Averaged statistics over all the sites within the two model domains and two sub-domains are presented. For the 42-km resolution run, the "eastern" sub-domain (region left of green line, Fig. 2b) is chosen to be compatible to the 15-km resolution domain for comparison purposes, and, for the 15-km resolution run, the "BAQS-Met" sub-domain is chosen to be somewhat comparable to the high-resolution 2.5-km resolution model domain focused to the intensive field study area.

The ozone mean biases (MB, Table 1) are positive for all domains and sub-domains, but decrease with increasing resolution. The mean biases for the model daily 1 h maximum, daily mean, and hourly values are all very similar for the same grids. The root mean square error also decreases with increasing resolution. The correlation coefficient decreases slightly with increasing resolution. The latter may reflect spatial misplacement of events becoming more frequent at higher resolution; the low resolution simulations being more likely to capture part of a "near-miss" transport event than high resolution.

ACPD
10, 14241–14312, 2010

3.2 AURAMS 2.5-km ozone versus mesonet and supersite ozone observations

Statistical comparisons between the 2.5-km/2-min AURAMS simulations and the mesonet stations shown in Fig. 3 are given in Table 2. In order to create a set of summary statistics across all stations (some of which had different averaging times), observed and modelled station values were first summed to create hourly averages, and the daily average, daily 1hr average maximum, daily 1hr average minimum were also constructed. In Table 2, the increase in model resolution considerably improved the model correlation coefficients relative to the lower resolution simulations of Table 1; mean biases, while now negative, are also of lower magnitude than the lower resolution simulations.

3.3 AURAMS 2.5-km ozone versus aircraft observations

Statistical comparisons between the 2.5-km/2-min AURAMS simulations and the entire sequence of flights, and for individual flights, to the aircraft observations, are shown in Table 3. The "All Flights" statistics show a correlation coefficient of 0.74, slope of 0.98, intercept of −7.4 ppbv, a mean bias of −8.4 ppbv, and a mean error of 12.3 ppbv. The correlation coefficients and slopes are improved relative to the monitoring network data in the aforementioned tables, though the biases have become more negative and the mean errors are similar to the monitoring network values. The high resolution model thus has the tendency to be biased lower for ozone aloft than at the surface. Individual flight statistics were generally worse than the overall evaluation due to their short duration and the impact of very local sources; 10 out of 16 flights having correlation coefficients (one sig. fig.) of less than 0.5. The flights with the lowest correlation coefficients tended to have large positive intercepts (e.g. Flights 6, 7, 14, each having $R < 0.0$, had the three largest positive intercepts of 62, 77, and 50 ppbv). Figure 4 shows the observed time series, simulated time series, correlation scores and mean biases for all flights. Most flights have negative mean biases; the model (thick line on the figures) is biased low relative to the observations (white diamonds).

ACPD
10, 14241–14312, 2010

Both the observations and the model show the presence of relatively short duration changes in the ozone concentration, indicating local-scale perturbations in the ozone field. For example, Flight 2 (Fig. 4b) shows peak-to-trough ozone concentration variations of 15 ppbv over durations of 4 min, Flight 14 (Fig. 4n) shows peak-to-trough variations of 30 ppbv over 26 min duration in the observations, while the model values show a similar magnitude range but over a shorter duration of about 8 min. The typical flying speed of the Twin Otter is 60 m s^{-1}, indicating that these ozone features have trough-to-trough spatial scales of 28 to 94 km. Superimposed on these are even shorter time interval events; for example, Flight 4 (Fig. 4d) shows two simulated peaks each of duration 6 min (21 km) with peak-to-trough variation of 20 ppbv, while the observed variation in the same part of the time series is about 12 ppbv. Both the observations and the model thus suggest the presence of small spatial-scale ozone features, and that accurate model simulations requires positioning errors of no greater than half of these durations and spatial scales.

To explore this issue further, the portion of Flight 2 (Fig. 4b) between 18:06 and 18:26 is examined in more detail in Fig. 5, which shows a close-up of the model and observed ozone time series, as well as the model-predicted ozone concentrations at 18:20 and 1235 and 1500 m a.g.l. (approximately 1435 m and 1700 m a.s.l.; the model levels closest to, and just above, the aircraft altitude during this portion of the flight). The observed ozone maximum is 52 ppbv, while the model maximum is 35 ppbv (Fig. 5a). The aircraft trajectory during the given time interval is shown on the figure as a dotted line arrow (Fig. 5b, c). The model predictions show low ozone concentrations due to titration in a power-plant plume (Lambton power-plant, Fig. 5, point marked "A" to the west of the flight track), slight ozone enhancement in the downwind region south of the plume over the north end of Lake St. Clair ("B"), and a weak ozone ridge between Lake St. Clair and Lake Erie ("C"). The model-predicted ozone concentration at the nearest model level (Fig. 5b) below the aircraft observations point B and C are 46 ppbv, and 37 ppbv, and 52 ppbv and 42 ppbv at the next level up (Fig. 5c). Comparing to the magnitudes of the two peaks in the observations during the flight (5a), with the location

ACPD
10, 14241–14312, 2010

of the local ozone maximum "B", one possible explanation for the underprediction in the model results may be a slight displacement in the predicted location of the ozone production region at point B relative to observations: the model under-prediction may be due in part to a 10-km horizontal (model too far west) and 1 layer vertical (model one level too high) error in the placement of the maximum at point B. It should be noted, however, that the statistical comparison shows that a systematic negative bias also occurs. The model peaks lead the observations by 2 min (or about 8 km distance at the flight speed of the twin otter). The model wind fields at the two levels bracketing the aircraft altitude are shown in Fig. 6: the complex nature of the local wind field in the vicinity of this portion of the flight track is shown. At the lower elevation, reversals in the wind direction occur just east of the start of the flight track, associated with a local anticyclonic circulation on the north-east shore of Lake St. Clair. The start of the flight track is in a region of low velocity horizontal wind shear at both levels in the model. On the south side of Lake St. Clair, the flight track crosses a region of diverging air, with rapid changes in wind direction. Figure 7 shows the observed wind direction time series for the observations along the flight track shown in Fig. 6, compared to the 18:00 UT model output. At the start of the time series, the model winds are more northerly than the observations, suggesting that the modelled anticyclonic circulation is placed about 10 to 20 km too far to the east relative to the observed atmosphere. The model wind fields at two levels over the lake shown in Fig. 7 (centre portion of the time series) suggest that the presence of significant changes in wind direction with height, and are generally within 30 degrees of the observations. The model suggests strong wind shears with height on the north and south sides of the lake; 30 to 45 degrees direction changes between 1210 and 1435 m a.s.l. Both model and observations agree on the location of the region of wind direction change at the southern end of the flight. The model's failure to predict the observed ozone peak's timing and magnitude during this flight segment (52 ppbv, 18:16 UT in reality, 35 ppbv, 18:12 UT in the model) may thus in part be due to (a) the predicted location of the anticyclonic circulation in the model being too far east, hence (b) the model NO_x plume (from point A in Fig. 5)

ACPD
10, 14241–14312, 2010

reaching further south than observed hence (c) the transition between ozone titration and ozone production occurs too far south in the model.

Another possible cause for the low model ozone relative to observations during this portion of the flight might be excessive titration from the NO_x source. Figure 8 compares observed and modelled NO during the entire flight: the model peaks match observed peaks in timing – these likely represent the NO plume from the Lambton power-plant, but the model magnitude is biased high, possibly due to the tendency for the winds model winds to be more northerly than observed. NO_x emissions for this power-plant were taken from continuous emissions monitoring data, suggesting that errors in the vertical placement and/or dispersion of the plume have occurred. The NO_x titration region associated with the plume may therefore be misplaced in the model simulation than in the real atmosphere, lowering the predicted ozone concentration.

The above examples illustrate the difficulties inherent in the creation of high spatial and time resolved simulations of ozone: the model performance over longer time periods is often much better than the performance for specific short term events. Small errors in the placement and timing of local circulation events may have a large impact on simulated concentrations along any given flight path. Despite this, the example shows that careful analysis of the model output allows a useful interpretation of the observations to be achieved: even when the model results do not correspond well to the observations at specific points along the flight path, the model predictions may be used to infer the main processes resulting in the observed ozone features.

3.4 AURAMS 2.5-km ozone versus ozonesonde observations

Ozonesonde observations were carried out at the Ridgetown supersite at 12 h intervals during the study. Model profiles were extracted from each horizontal resolution of the model simulations at the same times as the ozonesonde releases. The 2.5-km model results and the observations are compared in Fig. 9 for the intensive period. Both model and observations show a tropopause fold occurring at the start of the time period (20 June); ozone concentrations greater than 120 ppbv reach elevations as low

ACPD
10, 14241–14312, 2010

as 8 km a.g.l. in the observations. The model shows two later similar events, some indication of which may be present in the observations, but are difficult to distinguish due to missing data. In the model results, these high concentrations extend down to the 4-km level, while the observations show a shallower penetration, to about the 8-km level. Most of the measurement period shows a reasonable comparison between observations and model predictions. A detailed study of stratospheric/tropospheric exchange during the measurement intensive is presented in He et al. (2010).

The ozone predictions for this study at mid and upper tropospheric levels, and the dependence of these predictions on the manner in which upper and lateral boundary conditions are prescribed have been the focus of a separate research project, reported elsewhere in this issue (Makar et al., 2010, under review). Briefly, the best match between surface ozone network data and observations was found by modifying the vertical location of the profiles of ozone climatologies (Logan, 1999) in accord with the meteorological model's predicted tropopause height.

3.5 AURAMS 2.5-km ozone versus CRUISER observations

Ozone and other observations were made on the CRUISER mobile laboratory, in transit along roadways in the region, or parked along roadsides, observation sites, or in downtown Windsor. CRUISER driving routes during the intensive are shown in Fig. 10a, b and c compare model and observed O_3 and NO_2, respectively, for the entire period. AURAMS ozone along the CRUISER driving routes is generally biased low (comparing all two minute model values with corresponding averaged observations: mean bias −22 ppbv, mean error 26 ppbv, RMSE 32 ppbv, correlation coefficient (R) 0.56). Nitrogen dioxide was biased high (Fig. 10c), suggesting that the negative biases in the ozone values are the result of excessive NO_x titration of ozone in the model. These biases are much more negative than that seen at the surface mesonet stations (e.g. compare to Table 1, O_3 hourly average mean bias of −3.77 ppbv). The implication is that the model in its current form is unable to capture the very local mixing of freshly emitted NO_x associated with the roadways' mobile sources, but once the NO_x has

ACPD
10, 14241–14312, 2010

been dispersed to the more rural locations of the mesonet, the fit to the observations improves.

4 Model-predicted causes of ozone formation and destruction over the great lakes

4.1 Case studies

We turn now to the use of the model as an analysis tool to explain surface and lower troposphere ozone formation in the study region. During the three-week duration of the measurement intensive, specific patterns of circulation and ozone concentrations tended to recur, depending on the synoptic winds. Three specific patterns occurred with sufficient frequency to be useful as archetypes for the given circumstances for ozone formation. We examine these archetypes below with three case studies (additional case studies are examined in Levy et al., 2010).

4.1.1 26 June 2007: Lake St. Clair lake-breeze front enhancement of ozone north of detroit

The synoptic winds in this case are from the south-west. Mesoanalysis wind fields and lake-breeze front lines (the latter inferred from the measured winds as well as satellite cloud analysis and radar fine-line analysis, see Sills et al., 2010, under review) are shown in Fig. 11. South of Lake Erie, the lake-breeze front extends up to 50 km inland by 23:00 UTC (07:00 p.m. local daylight time). The lake-breeze front west of Lake Erie and the front from Lake St. Clair create a region of weak surface convergence to the west of Lake St. Clair. The Lake Huron front is pushed northwards over that lake by the synoptic flow. Figure 12 shows the corresponding wind fields and fronts (the latter inferred from convergence regions in the wind fields) predicted by GEM. There is a good correspondence in the locations of the main convergence lines in the vicinity

ACPD
10, 14241–14312, 2010

of the lakes between measurements and observations (compare Figs. 11 and 12), though GEM tended to overpredict convection during this period (gust fronts in Fig. 12). Figures 13a and 14a show the corresponding model-predicted ozone concentration fields at the same times. High concentration (>100 ppbv) ozone starts to appear by 02:00 p.m. local time (Fig. 13a), and continues to increase through 07:00 p.m. local time (14a).

Mass tracking of gas-phase production and loss versus total transport can be used to show that the ozone is created photochemically in the early afternoon, but later convergence downwind of the production region is responsible for further increases in the ozone concentration that occur thereafter (similar to the behind-front net convergence of ozone and precursors noted by Drobinski et al., 2007). Figure 13 shows the model-predicted 18:00 UT (02:00 p.m. local time) (a) surface gas-phase ozone concentrations, (b) ozone concentration and wind fields along a cross-section north of Detroit (A–B in 14a), (c) photochemical production and destruction of ozone along the cross-section, (d) total transport of ozone along the cross-section, (e) photochemical production and destruction along a second cross-section closer to Detroit (C–D), and total transport of ozone (advection+diffusion) along this second cross-section (f). Figures 13a, b show that high concentration ozone occurs in regions of surface convergence (points a, b along line A–B, Fig. 13a) and consequent lofting (points a and b, Fig. 13b, note upward wind vectors at these points). Ozone is photochemically created northeast of the city by photochemical production (13c and e, positive values), and is transported out of these photochemical production regions (13d and f, negative values; note the spatial correspondence between positive values in 13c and 13e, respectively). Figure 14 shows the same fields as Fig. 13, but at 23:00 UT (07:00 p.m. local time): gas-phase production has shut off along the cross-section (14c and 14e show no ozone production and small regions of surface titration), but ozone transport continues to move from the convergence region to its boundaries (14d and f) and forward along the direction of flow. By 07:00 p.m. a dome of high concentration ozone formed earlier to the west of Lake St. Clair (13e) has combined with the Detroit plume (14b) further downwind.

ACPD
10, 14241–14312, 2010

Note the wind-fields of Fig. 13b, which show the vertical transport associated with the surface convergence region.

Figures 13 and 14 predict that the region of greatest ozone formation on that day will be on the US side of the border. Observed surface ozone on 26 June is compared to model predictions in Fig. 15, for sites arranged from south to north near the border (Sombra station, Fig. 3, was not operating that day). Model and observations are within 15 ppbv at Paquette Corners (15a) and Bear Creek (15b), while the model is biased −46 ppbv during the ozone maximum at Grand Bend (15c). This large negative bias is apparently due to a small error in the wind direction. Figure 15d, e shows the model-predicted concentrations in the area at 18:00 UT and 23:00 UT, respectively, along with the three site locations. High ozone concentrations downwind of the Sarnia plume are predicted by the model in the *vicinity* of Grand Bend, but these remain off-shore for most of the day, and come on-shore to the north-east of the station, in contrast to the observations. The model results suggest that the high values are associated with the Lambton power plant plume.

This analysis has several common features with the other examples of model-predicted lake-breeze front ozone formation which follow in subsequent sections: (a) ozone photochemical production just outside precursor source regions (in subsequent analysis we show that on average these regions maximize over the lakes) in the early afternoon (b) lake-breeze fronts that result in local convergence of both ozone and precursors at the surface and subsequent lofting of these species in the frontal convergence zone, similar to Drobinski et al. (2007) (c) early evening increases in ozone concentration continuing in the convergence zones, despite photochemical production having shut down earlier.

4.1.2 8 July, 2007, 9 July 2007, 27 June, 2007: long-range transport of ozone along lake-breeze frontal convergence zones

27 June, 8 July and 9 July were days with “high deformation” lake breezes (Sills et al., 2010, under review); moderate south-westerly synoptic winds coupled with strong lake

ACPD
10, 14241–14312, 2010

breezes reaching far inland and downwind of the lakes themselves. 8 July is examined here as an example (note that Flight 15 on 8 July, Table 3, has the highest R value of the flight simulations). Figure 16a shows the mesoanalysis front locations and 16b shows the model-predicted wind fields and surface convergence regions at 17:00 UT (01:00 p.m. local time). A similar pattern is predicted (16b) – the model shows the front to the north of Lake St. Clair extending much further to the north-east compared to the mesoanalysis, but the latter was limited due to the lack of meteorological indicators to the south of Lake Huron. Figure 17 shows the model versus observations surface ozone comparison at two stations (Sombra, 17a, and Croton, 17b). The model is biased low for both stations at night. The model fit during the day is better at Sombra station, where both model and measurements show small time duration enhancements of ozone on the order of 20 ppbv at midday. Figure 18 shows the model-predicted ozone fields at the surface (18a) and two cross-sections, the first from North Detroit to Toronto (18b) and the second from Lake Huron to Lake St. Clair (18c). The ozone concentrations at the surface (18a) show an elongated feature of high ozone along the more northern of the two convergence lines through southern Ontario. The Detroit – Toronto cross-section (18b) shows: ("A") high ozone concentrations from the surface through elevations up to 1500m north of Lake St. Clair, ("B") a second region of high ozone further downwind, ("C") a region where high ozone concentrations occur aloft, and ("D") the high ozone concentrations reaching the locally-produced ozone of the city of Toronto. The cross-section between Lake Huron and Lake Erie across this feature ("E" to "F") suggests that high concentration ozone is associated with helical circulation in the vicinity of the lake-breeze fronts (Fig. 18a, b shows that the wind field is largely aligned along the length of the convergence zone, while 18c, looking in the direction of that flow, shows a clockwise circulation at 1000 m aloft at "B", with plumes of ozone becoming detached from the surface in response to these circulation patterns. This helical transport pattern has been noted in other high resolution model simulations (Lyons et al., 1995).

The model's corresponding predictions for gas-phase photochemical production and

ACPD
10, 14241–14312, 2010

loss, and total transport, are shown in Fig. 19. The panels of Fig. 19 show that ozone is photochemically created (Fig. 19a, c) between the surface and heights of 1600 m above the surface, near the cities and downwind of the region north of Lake St. Clair. The ozone production regions are sometimes detached from the surface, with maxima between 1000 and 1400 m. Figure 19c also shows significant ozone production occurring near the surface over Lake Huron. Transport (both horizontal and vertical) is removing ozone from these photochemical production regions (note correspondence of blue areas, Fig. 19b, d, to red areas, 19a, c). Transport increases the ozone concentrations at elevations above 1600 m and downwind and adjacent to the photochemical production areas (red areas, 19b, d). Three dimensional surface plotting of the transport terms suggests that they are driven by the local flow rather than the synoptic winds; the highest transport levels are along the convergence line.

As in Sect. 4.1.1, the above analysis suggests that the surface convergence zones associated with lake breezes will increase photochemical ozone production just downwind of precursor source regions by confining and hence increasing precursor concentrations in the convergence region, similar to the findings of Drobinski et al. (2007). Ozone concentrations are also enhanced even further downwind via transport of ozone and its precursors along the convergence line. Extended features of high concentration ozone may become detached from the surface, and travel considerable distances (hundreds of km) downwind of the source regions. These ozone plumes may eventually fumigate downwards, depending on conditions further downwind (for example, the ozone aloft might be brought to the surface on a subsequent day during boundary layer growth, or the ozone aloft may be caught up in a downwind urban heat island circulation).

While these regions of enhanced ozone are relatively small (10's of km across, though up to 250 km long, in the above example), and may be difficult to accurately position relative to the ambient atmosphere, observations from the mesoscale monitoring network sometimes capture very similar features in the ozone time series. An example of this can be seen in the measurement record for 9 July. Figure 20 shows the

ACPD
10, 14241–14312, 2010

observed (green) and simulated (blue) time series at Croton (20a) and Sombra (20b). The Croton time series (20a) shows that the model captures a Lake St. Clair-derived ozone event (circled in red) very well, lagging the observations by about an hour, but getting close to the same magnitude and shape of the observed event. In contrast, the Sombra observation time series shows that only one event was sampled, while the model ozone has enhanced ozone both before and after the observed event. Figure 21 shows the model-predicted surface ozone concentrations and wind fields downwind of Lake St. Clair on 9 July at 17:00, 19:00, 20:00, and 22:00 UT and 20:00 UT (1, 3, 4 and 06:00 p.m. local time, respectively), as well as the locations of the two ozone surface stations corresponding to the time series of Fig. 20. From 17:00 through 19:00 UT (Fig. 21a, b), Sombra station (SOM) experiences high ozone associated with a region on the north side of Lake St. Clair. Very high ozone concentrations (>100 ppbv) build up in the region of surface divergence over the lake itself, at 17:00 UT (21a). This high ozone region intensifies and is advected NE over Lake St. Clair (21b), resulting in the 20 ppbv ozone "spike" in the observation record at 20:00 UT (21c, 20a). The subsequent drop in ozone concentrations at both stations results from NO_x titration from the Lambton plume at Sombra, and a larger scale decrease at Croton (21d). Mass tracking of the ozone formation and loss processes (not shown) for these times shows that the ozone is photochemically created on the west side of Lake St. Clair – the high ozone concentration pattern in Fig. 21 is mostly the result of the local circulation pattern. The better fit of the model time series at Croton (Fig. 20a) than at Sombra (20b) suggests that the earlier 17:00 UT "north of Lake St. Clair" event and the later, "Lake St. Clair divergence" event at Sombra (Fig. 21a, b, d) are biased high in the model simulation. Croton station does not experience the first event, but does experience the second. The observation time series shows that very local events associated with lake circulation are capable of enhancing the ozone concentrations by about 20 ppbv relative to the surrounding regions. The model simulations suggest that these events are closely linked to the local circulation in the vicinity of the Lakes. Further comparisons follow in Sect. 4.2.

ACPD
10, 14241–14312, 2010

4.1.3 5 July, 6 July 2007: Lake St. Clair ozone production dome

The last of the three circulation patterns observed in the model output is associated with photochemical processing over, and transport from, Lake St. Clair. Figure 22 shows the model ozone and wind fields (Fig. 22a, c, e) and Croton (22b), Lighthouse Cove (22d) and Leamington (22f) observed and modelled ozone time series on 6 July. The concentration contours and wind fields suggest that each of these sites experiences ozone from different sources, Croton (22b) largely from production downwind of the Lambton and Sarnia emissions sources being carried south by the Lake Huron lake-breeze front (note convergence of wind fields north-west of station CRO in Fig. 22a and 22c). Lighthouse Cove (22d), meanwhile, experiences the outflow from ozone build-up over Lake St. Clair (22c). Leamington experiences flow from Lake Erie and from Detroit. Croton time series (22b) show a "plateau" of ozone concentrations of greater duration in the observations than the model simulation. Lighthouse Cove (22d) maxima are biased high relative to the observations; the model overpredicts the ozone concentrations exiting Lake St. Clair. At Leamington (22f), the model and observed ozone maxima are very similar, though the model is biased low for the period 13:00 EDT to 18:00 EDT (17:00 to 22:00 UT). The likely reason for this low bias is shown in Fig. 23, which compares the mesoanalysis for that area (23a) to the model-predicted wind fields on the same day (23b). The observed winds (23a) suggest that the model Lake Erie lake-breeze front penetrates insufficiently far inland compared to observations (compare front symbols in 23a to convergence lines in 23b). Figure 23c shows the gas-phase ozone and destruction predicted by the model at the same time; stronger advection from Lake Erie may move the Detroit titration/production line further west in the ambient atmosphere than in the simulation, and allow the Lake Erie ozone production region to come on-shore. The model low bias between 17:00 UT and 22:00 UT in Fig. 22f may therefore be the result of insufficient Lake Erie ozone being advected onto land in the model simulation.

ACPD
10, 14241–14312, 2010

4.2 Local ozone events: detailed comparison to the surface network

The surface network described earlier can be used to determine the extent to which the local ozone features (which the model suggests are the result of local circulation-chemistry interactions) may be occurring in the ambient atmosphere. The following examples were taken by scanning through the model surface ozone and wind field output for cases of ozone enhancement due to lake-breeze circulation, noting the stations where these features would impact, then comparing the model and observed ozone time series for those stations at those times.

4.2.1 8 July: ozone transport event at Sombra (SOM), Bear Creek (BEA), Leamington (LEA) stations

Model-generated surface ozone and wind fields at 17:00, 18:00 and 20:00 UT (01:00, 02:00, 04:00 p.m. local time), and the time series for the above stations are shown in Fig. 24. The surface ozone and wind maps (Fig. 24a, c, e) show high concentration ozone forming along a frontal convergence line through and north-east of Sombra station, and another lower concentration feature north-east of Leamington station forms by the end of this sequence (24e). The time series for Sombra (24b) shows that the model overpredicts high ozone and underpredicts low ozone during the 24 h interval depicted. The model accurately predicts the timing of the main peak, as well as the local enhancement of ozone between 14:30 and 15:00 EDT of about 10–15 ppbv corresponding to the time when the convergence line places high ozone immediately over the station in the model simulation. At Bear Creek (24d), both observations and model show a double peak in the ozone maxima, but the second peak in the model lags the observations by about 2 h and is of lower magnitude than the observations. The observations show local enhancements of 1 h duration of 10 to 20 ppbv at times when the model predicts ozone leaving the Lake St. Clair shoreline in a narrow (10 to 15 km wide) convergence zone. The time series comparison for Leamington (24f) shows a reasonable agreement between observations and measurements for the daytime max-

ACPD
10, 14241–14312, 2010

ima, though the model lags the observations for the location of the maximum by about an hour. The model simulations (24e) suggest that the Sombra/Bear Creek maximum has a different source than the Leamington maximum, with the former resulting from emissions in Detroit creating ozone over Lake St. Clair, and the latter resulting from photochemical production over Lake Erie. All three time series suggest that the model is biased low in the early morning, possibly indicating excessively high ozone titration by NO_x in the simulations.

4.2.2 9 July: ozone transport event at Bear Creek (BEA), Palmyra (PAL) and Leamington (LEA) stations

Figure 20 compares observations to model values at Croton and Sombra stations; here (Fig. 25), comparisons are made with three additional stations on the same day. Figure 25a, c, e shows model-predicted ozone and wind-fields at 17:00, 19:00, 22:00 UT and the locations of the three stations, while model and observed ozone time series for each station are shown in Fig. 25b, d, f.

Bear Creek station (25b) shows good agreement with the observed ozone; the timing, magnitude and shapes of the first two peaks are very similar. The first and second peaks (model 17:00 UT/13:00 EDT and 19:00 UT/15:00 EDT respectively, Fig. 25a, c) correspond to times when the model predicts the Lake St. Clair ozone maxima touches the shoreline, pulls back (at 18:00 UT), then comes ashore (19:00 UT). The third model peak (absent from the observations which instead show constant elevated concentrations) at 21:30 UT/17:30 EDT suggests that the high concentration ozone generated over and on the north side of Lake St. Clair remains in the Bear Creek area longer in the observations than in the simulation.

Palmyra (Fig. 25d) shows a reasonable fit to the observations, though Palymyra model values lead the observations by about 2 h. The Leamington model values are biased about 20 ppbv low. The model surface maps (25a, c, e) suggest that Leamington (25f) at this time was being affected by ozone originating from different sources, from both southern Detroit and western Lake Erie, which may account for the multiple peaks

ACPD
10, 14241–14312, 2010

in the observations and simulated by the model. The model concentrations at Palmyra are due to the same sources as Leamington, advected further downwind.

4.2.3 10 July: transport of Detroit/Lake St. Clair ozone to Lake Huron, stations Bear Creek (BEA), Croton (CRO), Sombra (SOM) and Grand Bend (GRB)

In this example, high ozone concentrations are generated on the north side of Lake St. Clair and are carried to the north-east to the shores of Lake Huron. Model surface ozone concentrations at 17:00, 18:00, and 19:00 UT (13:00, 14:00, 15:00 EDT) are shown in Fig. 26a, c, e. The time series for stations from north to south (GRB, SOM, CRO and BEA) are shown in Fig. 26b, d, e, and g respectively. Figure 27 compares the model-generated wind fields (with convergence lines and gust fronts highlighted) with the mesoanalysis at the same three hours. The model captures the high concentrations at Grand Bend (26b), with a similar magnitude maxima that lags the observations by an hour. Subsequent model concentrations are biased 15 ppbv high – the surface concentration fields (26 a, c, f) show that Grand Bend is on the edge of a lake-breeze front on the south side of Lake Huron, with a rapid change of concentration in the vicinity of the front. The comparison to the mesoanalysis in the vicinity of Grand Bend (Fig. 27) shows that the high concentrations at this site are strongly influenced by the location of the Lake Huron front; a 10–15 km difference in the placement of the front is capable of accounting for the concentration difference between model and observations. The time series at Sombra station (26d) shows a very good agreement with observations, with the same 1 h lag in the arrival of the maximum. The model time series at Croton station (26f) also shows a very good agreement with observations, with a negative bias of about 10 ppbv. Both model and observations at Croton and Bear Creek have maxima at or below 80 ppbv, while Sombra and Grand Bend, both in the influence of the convergence zones and the Lake St. Clair/Detroit ozone production region, have higher ozone concentrations. The pattern of predicted wind fields and frontal convergence lines (Fig. 27a, c, e) is very similar to that of the mesoanalysis (27b, d, f). Overall, this case gives good evidence for the enhancement of ozone due to lake-breeze frontal

ACPD
10, 14241–14312, 2010

convergence zones, and the transport of events created in these zones over distances on the order of 150 km.

4.3 Averages of model fields: the average impact of transient events

The events described above are transient in that they may last over the course of a few hours. In order to determine the impact of these transient events over a longer time frame, hourly model output for the ozone concentration, mass tracking fields and winds for the 23 days of the intensive were averaged by UT hour. These averages show that the lake-breeze fronts have a consistent average diurnal pattern, and a significant effect on local ozone production.

4.3.1 UT hour-average surface horizontal winds

The synoptic flow is from the south-west during the intensive. Wind features associated with the lake-breeze fronts appear in the afternoon. Figure 28 shows the 23 day averages of the surface wind field at 12:00, 16:00, 20:00 and 00:00 UT (08:00 a.m., 12:00 p.m., 04:00 p.m., and 08:00 p.m. local time). By noon (Fig. 28b), lake-breeze convergence zones (solid mauve lines) appear on the south west shore of Lake Huron, west shore of Lake St. Clair, the west and north shores of Lake Erie, and the north shore of Lake Ontario. Each of these lakes in Fig. 28b also contains a region of surface divergence; the outflow from this divergence region perturbs the synoptic flow (limits of this outflow region are indicated by dashed mauve lines). The convergence zones persist through 04:00 p.m. (28c), and the outflow regions push considerable distances inland. By 08:00 p.m. (28d) the impact of the lake breezes becomes harder to discern; the average wind speed being sufficiently small to preclude plotting in several locations, probably indicating significant variability in the duration and direction of the surface divergence over the lakes by this time in the evening. The figure shows that the lake-breeze fronts are sufficiently robust features that they affect the hourly average wind circulation over the lakes.

ACPD
10, 14241–14312, 2010

4.3.2 UT hour-average ozone concentrations

Time-averaged surface ozone concentrations for the same hours as Fig. 28 are shown in Fig. 29. The most significant high concentration ozone features are over Lake Erie, and over the region shared by Detroit, Windsor, and Lake St. Clair (at 04:00 p.m., Fig. 29c). The former shows higher ozone on the US than on the Canadian side of Lake Erie – this is due to differences in the emissions databases for the two countries (in Canada, shipping emissions are spatially allocated only along the main shipping lines, in the US, some shipping emissions are spread out over the south side of Lake Erie). The large differences across the border suggest that accurate spatial allocation of shipping emissions is essential for forecasting ozone production over the great lakes, and that those emissions may have a significant effect on local ozone production.

The average Lake St. Clair surface ozone at 04:00 p.m. (29c) is clearly enhanced within the region of the lake-breeze convergence line and surface outflow (28c). However, it is difficult to distinguish any effect of the longer convergence lines discussed earlier, probably due to their relatively short duration and highly time-varying positions, though some features do suggest their presence in the average. Figure 29b shows enhanced ozone concentrations (>45 ppbv) along the northern Lake Erie coastline and inland, matching the line of the convergence zone of Fig. 28b. A similar isolated high ozone feature in Fig. 29b matches the location of the Lake Huron outflow and Lake St. Clair convergence line of Fig. 28b.

In order to examine the average ozone over Lakes St. Clair and Erie in more detail, the 23 day average 16:00 UT ozone concentrations at the surface over the lake, as well as the corresponding cross-sections of ozone concentration, ozone gas-phase production and loss and ozone transport are shown in Fig. 30a–d. The size of each lake has a significant effect on the ozone production reaction; over Lake St. Clair (left side of cross-sections, 30b), the region of enhanced average ozone extends to elevations of greater than 1500 m, while the enhanced ozone production over Lake Erie rises to no more than 250 m above the surface. Figure 30c shows that gas-phase photochemical

ACPD
10, 14241–14312, 2010

production of ozone is the source of the high concentrations, but once again, the Lake St. Clair source (left side of the cross-section, 30c) has a much greater vertical extent than that over Lake Erie (right side of the cross-section, 30c). The average local gas-phase production rates are relatively high, up to 5 ppbv/hour. The transport pattern (30d) differs between the two lakes. For Lake Erie, transport removes ozone in a thin layer near the surface, and a narrow region of ozone removal extending up to 1500 m is flanked by regions of positive ozone transport. The region of transport removal for Lake St. Clair is larger in horizontal extent, suggesting that at least some of direction of transport is not in the plane of the cross-section.

Figures 28 to 30 suggest that the local diurnal circulation associated with the two Lakes is sufficiently strong to be present in the 23 day average wind fields (28), that this circulation affects the ozone concentrations (29), that the Lakes are photochemical ozone production regions (30), the Lake St. Clair source being a dome roughly 1500 m in height and ~30 km in diameter, and the Lake Erie source being relatively shallow (250 m altitude), but encompassing much of the S.W. side of the Lake. A cross-section of the simulated 3-D wind field through the 23 day averages across both lakes is shown in Fig. 31, and shows how differences in the circulation over each lake gives rise to their differences in the vertical distribution of gas-phase ozone production. At 08:00 a.m. (Fig. 31a), vertical winds are relatively light. By noon (31b), a strong vertical circulation has developed. Updrafts over the north-west shore of Lake St. Clair, likely partially driven by the Detroit heat island ("A" to "B"), and downdrafts over the lake ("B" to "C"), have formed a helical circulation with the synoptic flow, and may allow a recirculation of pollutants over Lake St. Clair. A smaller helical recirculation pattern occurs aloft over Lake Erie, but the larger size of this lake results in net subsidence near the surface. The wind barbs suggest that some air aloft may also reach Lake St. Clair (though the synoptic wind is roughly perpendicular to this cross-section, so the opportunity for the air over Lake Erie to reach Lake St. Clair may be small). By 04:00 p.m. (Fig. 31b), the Lake St. Clair vertical circulation has intensified and moved southwards, so that the updraft is now on the western shore of the lake itself. The land between the two

ACPD
10, 14241–14312, 2010

lakes has become an intense updraft, due to daytime surface heating. These vertical (*re*) circulations explain the difference in the elevations of the ozone production regions noted above (Fig. 30), and similar features have been noted in the literature (Levy et al., 2008).

The main sources of emissions near Lake St. Clair are the cities of Detroit and Windsor; precursor concentrations will be vertically distributed and re-circulated over Lake St. Clair. The Lake Erie region is heavily influenced by shipping emissions, and the large emission sources on the sourthern shore of Lake Erie. These emissions are emitted over the lake itself, and along its shoreline, and are trapped within the lake's stable marine boundary layer (which is much more stable than that of Lake St. Clair due to the relative sizes of the two lakes). Differences in ozone production between the Canadian and US sides of the border over Lake Erie reflect differences in the spatial allocation of the emissions data for each country (Fig. 30a, compare north versus south sides of Lake Erie on the east side of the panel; the emissions inventory, not shown, includes emissions spread over the lake on the south side of the border, while only on the main shipping lane on the north side).

5 Conclusions

The simulations and comparisons with observations performed here suggest that ozone formation over the southern Great Lakes is significantly enhanced by local circulation and photochemical processing of precursors. Lakes Erie and St. Clair frequently act as photochemical production regions, with average enhancements on the order of 6 to 8 ppbv per hour by early afternoon. The lake-breeze circulation may lead to the formation of elongated features of high concentration ozone extending several hundred kilometres, over the course of a day. These features originate downwind of the urban emissions source regions, and over the photochemical production regions of the Lakes. Surface convergence of the local circulation carries the ozone and its precursors aloft and the synoptic wind thus carries the ozone much further downwind.

ACPD
10, 14241–14312, 2010

The results have important implications for ozone forecasting in this region. Current air pollution model forecasts generated by the Canadian and US governments operate on 15- and 12-km resolutions, respectively. These resolutions are insufficient to adequately resolve the lake-breeze circulations – while the high-resolution simulations performed here suggest that these same circulations may be responsible for enhancements of the regional ozone concentrations by ~20 ppbv. The photochemical source regions over Lakes St. Clair and Erie are sufficiently robust features that the long-term average ozone is affected, while the elongated features in the frontal zones are sufficiently infrequent to have a less significant effect on the average ozone. Cross-sections of the 23-day average wind fields show that Lake St. Clair is affected by a vertical recirculation that may enhance its ozone production, and Lake Erie's high ozone concentrations result from strong subsidence over the lake. The local nature of these features suggests that very local-scale emissions controls may have a significant impact on ozone concentrations in this region.

The statistical comparison with observations shows that the model forecast is significantly improved in going from 15- to 2.5-km resolution. Shorter time interval comparison to the observations show a decrease in accuracy – the model on average performs much better than on specific days or for specific events, particularly for the measurements aloft. Further improvements to high resolution forecast accuracy may be possible, using the case-studies outlined here to gauge improvements to circulation and chemical algorithms.

Acknowledgements. The authors would like to acknowledge the financial support of Environment Canada and the Ontario Ministry of the Environment for the BAQS-Met study. We gratefully acknowledge the assistance of the AIRNow program and its participating stakeholders.

References

Anlauf, K. G., Lusis, M. A., Wiebe, H. A., and Stevens, R. D. S.: High ozone concentrations measured in the vicinity of Toronto, Canada, Atmos. Environ., 9, 1137–1139, 1975.

ACPD
10, 14241–14312, 2010

Banta, R. M., Senff, C. J., Nielsen-Gammon, J., Darby, L. S., Ryerson, T. B., Alvarez, R. J., Sandberg, S. R., Williams, E. J., and Trainer, M.: A bad air day in Houston, B. Am. Meteorol. Soc., 86(5), 657–669, 2005.

Bastin, S. and Drobinski, P.: Sea-breeze-induced mass transport over complex terrain in south-eastern France: A case-study, Q. J. Roy. Meteorol. Soc., 132(615), 405–423, 2006.

Byun, D. W., Kim, S.-T., and Kim, S.-B.: Evaluation of air quality models for the simulation of a high ozone episode in the Houston metropolitan area, Atmos. Environ., 41(4), 837–853, 2007.

CEP: Carolina Environmental Program, Sparse Matrix Operator Kernel Emission (SMOKE) modelling system, University of North Carolina, Carolina Environmental Programs, Chapel Hill, NC, online available at: http://www.smoke-model.org/index.cfm, 2003.

Cheng, F.-Y. and Byun, D. W.: Application of high resolution land use and land cover data for atmospheric modeling in the Houston-Galveston metropolitan area, Part I: Meteorological simulation results, Atmos. Environ., 42(33), 7795–7811, 2008.

Cheng, F.-Y., Kim, S., and Byun, D. W.: Application of high resolution land use and land cover data for atmospheric modeling in the Houston-Galveston Metropolitan area: Part II. Air quality simulation results, Atmos. Environ., 42(20), 4853–4869, 2008.

Cheng, W.-L.: Ozone distribution in coastal central Taiwan under sea-breeze conditions, Atmos. Environ., 36(21), 3445–3459, 2002.

Cho, S., Makar, P. A., Lee, W. S., Herage, T., Liggio, J., Li, S. M., Wiens, B., and Graham, L.: Evaluation of a unified regional air-quality modeling system (AURAMS) using PrAIRie2005 field study data: The effects of emissions data accuracy on particle sulphate predictions, Atmos. Environ., 43, 1864–1877, 2009.

Côté, J., Gravel, S., Méthot, A., Patoine, A., Roch, M., and Staniforth, A.: The operational CMC-MRB Global Environmental Multiscale (GEM) model. Part 1: Design considerations and formulation, Mon. Weather Rev., 126, 1373–1395, 1998.

Darby, L. S.: Cluster analysis of surface winds in Houston, Texas, and the impact of wind patterns on ozone, J. Appl. Meteorol., 44(12), 1788–1806, 2005.

Darby, L. S., McKeen, S. A., Senff, C. J., White, A. B., Banta, R. M., Post, M. J., Brewer, W. A., Marchbanks, R., Alvarez II, R. J., Peckham, S. E., Mao, H., and Talbot, R.: Ozone differences between near-coastal and offshore sites in New England: Role of meteorology, J. Geophys. Res. D, 112(16), D16S91, doi:10.1029/2007JD008446 2007.

Drobinski, P., Saïd, F., Ancellet, G., Arteta, J., Augustin, P., Bastin, P., Brut, A., Caccia, J.

ACPD
10, 14241–14312, 2010

L., Campistron, B., Cautenet, S., Colette, A., Coll, I., Corsmeier, U., Cros, B., Dabas, A., Delbarre, H., Dufour, A., Durand, P., Guénard, V., Hasel, M., Kalthoff, N., Kottmeier, C., Lasry, F., Lemonsu, A., Lohou, F., Masson, V., Menut, L., Moppert, C., Peuch, V. H., Puygrenier, V., Reitebuch, O., and Vautard, R.: Regional transport and dilution during high-pollution episodes in southern France: Summary of findings from the Field Experiment to Constraint Models of Atmospheric Pollution and Emissions Transport (ESCOMPTE), J. Geophys. Res. D, 112(13), D13105, doi:10.1029/2006JD007494, 2007.

Gipson, G. L.: Chapter 16, Process Analysis, in Science Algorithms of the EPA Models-3 Community Multiscale Air Quality (CMAQ) Modeling System, edited by: Byun D. W. and Ching, J. K. S., United States Environmental Protection Agency, Office of Research and Development, Washington, DC, EPA/600/R-99/030, 512 pp., 1999.

Gong, W., Dastoor, A. P. , Bouchet, V. S. , Gong, S. , Makar, P. A., Moran, M. D., Pabla, B. , Ménard, S. , Crevier, L.-P., Cousineau, S., and Venkatesh, S.: Cloud processing of gases and aerosols in a regional air quality model (AURAMS), Atmos. Res., 82, 248–275, 2006.

Hastie, D. R., Narayan, J., Schiller, C., Niki, H., Shepson, P. B., Sills, D. M. L., Taylor, P. A., Moroz, Wm. J., Drummond, J. W., Reid, N., Taylor, R., Roussel, P. B., and Melo, O. T.: Observational evidence for the impact of lake breeze circulation on ozone concentrations in southern Ontario, Atmos. Environ., 33, 323–335, 1999.

Hayden, K., Sills, D. M. L., Li, S., Brook, J., Anlauf, K. G., O'Brien, J. and Sharma, S.: The impact of lake breezes on trace gases and particles during the Border Air Quality and Meteorology Study (BAQS-Met), Atmos. Chem. Phys. Discuss., in preparation, 2010.

He, H., Tarasick, D. W., Hocking, W. K., Carey-Smith, T. K., Rochon, Y., Zhang, J., Makar, P. A., Osman, M., Brook, J., Moran, M. D., Jones, D., Mihele, C., Wei, J. C., Osterman, G., Argall, P. S., McConnell, J., and Bourqui, M.: Transport analysis of ozone enhancement in southern Ontario during BAQS-Met, Atmos. Chem. Phys. Discuss., accepted, 2010.

Houyoux, M. R., Vukovich, J. M., Coats Jr., C. J., and Wheeler, N. J. M.: Emission inventory development and processing for the Seasonal Model for Regional Air Quality (SMRAQ) project, J. Geophys. Res., 105, 9079–9090, 2000.

Jang, J.-C. C., Jeffries, H. E., and Tonnesen, S.: Sensitivity of ozone to model grid resolution – II. Detailed process analysis for ozone chemistry, Atmos. Environ., 29, 3101–3114, 1995.

Jeffries, H. E. and Tonnesen, S.: A comparison of two photochemical reaction mechanisms using mass balance and process analysis, Atmos. Environ., 28, 2991–3003, 1994.

Laird, N. F., Kristovich, D. A. R., Liang, X.-Z., Arritt, R. W., and Labas, K.: Lake Michigan

ACPD
10, 14241–14312, 2010

lake breezes: climatology, local forcing, and synoptic environment, J. Appl. Meteorol., 40(3), 409–424, 2001.
Lasry, F., Coll, I., and Buisson, E.: An insight into the formation of severe ozone episodes: Modeling the 21/03/01 event in the ESCOMPTE region, Atmos. Res., 74(1–4), 191–215, 2005.
Lemonsu, A., Bastin, S., Masson, V., and Drobinski, P.: Vertical structure of the urban boundary layer over Marseille under sea-breeze conditions, Bound.-Lay. Meteorol., 118(3), 477–501, 2006a.
Lemonsu, A., Pigeon, G., Masson, V., and Moppert, C.: Sea-town interactions over Marseille: 3-D urban boundary layer and thermodynamic fields near the surface, Theor. Appl. Climatol., 84(1–3), 171–178, 2006b.
Levy, I., Makar, P. A., Sills, D., Zhang, J., Hayden, K. L., Mihele, C., Narayan, J., and Brook, J.: Unravelling the complex local scale flows influencing ozone patterns in the southern Great Lakes, Atmos. Chem. Phys. Discuss., in preparation, 2010.
Levy, I., Dayan, U., and Mahrer, Y.: A five-year study of coastal recirculation and its effect on air pollutants over the East Mediterranean region, J. Geophys. Res. D, 113(16), D16121, doi:10.1029/2007JD009529 2008.
Li, S. M.: A concerted effort to understand the ambient particulate matter in the Lower Fraser Valley: The Pacific 2001 Air Quality Study, Atmos. Environ., 38(34), 5719–5731, 2004.
Logan, J. A.: An analysis of ozonesonde data for the troposphere: Recommendatioins for testing 3-D models, and development of a gridded climatology for tropospheric ozone, J. Geophys. Res., 104, 16115–16149, 1999.
Lu, R. and Turco, R. P.: Air Pollutant Transport in a Coastal Environment – II. Three-Dimensional Simulations over Los Angeles Basin, Atmos. Environ., 29, 1499–1518, 1995.
Lyons, W. A. and Cole, H. S.: Fumigation and Plume Trapping on the Shores of Lake Michigan During Stable Onshore Flow, J. Appl. Meteorol., 12, 494–510, 1973.
Lyons, W. A. and Cole, H. S.. Photochemical Oxidant Transport: Mesoscale Lake Breeze and Synoptic-Scale Aspects, J. Appl. Meteorol., 15, 733–743, 1976.
Lyons, W. A. and Olsson, L. E.: Detailed Mesometeorological Studies of Air Pollution Dispersion in the Chicago Lake Breeze, Mon. Weather Rev., 101, 387–403, 1973.
Lyons, W. A., Pielke, R. A., Tremback, C. J., Walko, R. L., Moon, D. A., and Keen, C. S.: Modeling Impacts of Mesoscale Vertical Motions upon Coastal Zone Air Pollution Dispersion, Atmos. Environ., 29, 283–301, 1995.

ACPD
10, 14241–14312, 2010

Lyons, W. A., Keen, C. S., and Schuh, J. A.: Modeling mesoseale diffusion and transport processes for releases within coastal zones during land/sea breezes. U.S. Nuclear Regulatory Commission, NUREG/CR-3542, Washington, DC, 202 pp., 1983.
Makar, P. A., Gravel, S., Chirkov, V., Strawbridge, K. B., Froude, F., Arnold, J., and Brook, J.: Heat flux, urban properties, and regional weather, Atmos. Environ., 40, 2750–2766, 2006.
Makar, P. A., Moran, M. D., Zheng, Q., Cousineau, S., Sassi, M., Duhamel, A., Besner, M., Davignon, D., Crevier, L.-P., and Bouchet, V. S.: Modelling the impacts of ammonia emissions reductions on North American air quality, Atmos. Chem. Phys., 9, 7183–7212, doi:10.5194/acp-9-7183-2009, 2009.
Makar, P. A., Gong, W., Mooney, C., Zhang, J., Davignon, D., Samaali, M., Moran, M. D., He, H., Tarasick, D. W., Sills, D., and Chen, J.: Dynamic ozone boundary conditions for air-quality forecasts, Atmos. Chem. Phys. Discuss., in press, 2010.
Marchuk, G. I.: Methods of numerical mathematics, Springer-Verlag, New York, 316 pp., 1975.
Mestayer, P. G., Durand, P., Augustin, P., Bastin, S., Bonnefond, J.-M., Bénech, B., Campistron, B., Coppalle, A., Delbarre, H., Dousset, B., Drobinski, P., Druilhet, A., Fréjafon, E., Grimmon, C. S. B., Groleau, D., Irvine, M., Kergomard, C., Kermadi, S., Lagouarde, J.-P., Lemonsu, A., Lohou, F., Long, N., Masson, V., Moppert, C., Noilhan, J., Offerle, B., Oke, T. R., Pigeon, G., Puygrenier, V., Roberts, S., Rosant, J.-M., Saïd, F., Salmond, J., Talbaut, M., and Voogt, J.: The Urban Boundary-Layer Field Campaign in Marseille (UBL/CLU-ESCOMPTE): Set-Up and First Results, Bound.-Lay. Meteorol., 114, 315–365, 2005.
Millán, M. M., Salvador, R., Mantilla, E., and Kallos, G.: Photooxidant dynamics in the Mediterranean basin in summer: Results from European research projects, J. Geophys. Res., 102, 8811–8823, 1997.
Millán, M. M., Mantilla, E., Salvador, R., Carratalá, A., Sanz, M. J., Alonso, L., Gangoiti, G., and Navazo, M.: Ozone cycles in the western Mediterranean basin: interpretation of monitoring data in complex coastal terrain, J. Appl. Meteorol., 39, 487–508, 2000.
Mukammal, E. I.: Ozone as a cause of tobacco injury, Agr. Meteorol., 2, 145–165, 1965.
Mukammal, E. I., Neumann, H. H., and Gillespie, T. J.: Meteorological Conditions Associated with Ozone in Southwestern Ontario, Canada. Atmos. Environ., 16, 2095–2106, 1982.
Mukammal, E. I., Neumann, H. H., and Nichols, T. R.: Some Features of the Ozone Climatology of Ontario, Canada and Possible Contributions of Stratospheric Ozone to Surface Concentrations, Arch. Met. Geoph. Biocl., 34, 179–211, 1985.
Pirovano, G., Coll, I., Bedogni, M., Alessandrini, S., Costa, M. P., Gabusi, V., Lasry, F., Menut,

ACPD
10, 14241–14312, 2010

L., and Vautard, R.: On the influence of meteorological input on photochemical modelling of a severe episode over a coastal area, Atmos. Environ., 41(30), 6445–6464, 2007.
Puygrenier, V., Lohou, F., Campistron, B., Saïd, F., Pigeon, G., Benech, B., and Serça, D.: Investigation on the fine structure of sea-breeze during ESCOMPTE experiment, Atmos. Res., 74(1–4), 329–353, 2005.
Rappenglück, B., Perna, R., Zhong, S., and Morris, G. A.: An analysis of the vertical structure of the atmosphere and the upper-level meteorology and their impact on surface ozone levels in Houston, Texas, J. Geophys. Res. D, 113(17), D17315, doi:10.1029/2007JD009745, 2008.
Sills, D., Brook, J., Taylor, P., Zhang, J., Levy, I., Makar, P. A., and Hayden, K.: Lake breezes in the southern Great Lakes and their influence during BAQS-Met2007, Atmos. Chem. Phys. Discuss., in preparation, 2010.
Smyth, S. C., Jiang, W., Roth, H., Moran, M. D., Makar, P. A., Yang, F., Bouchet, V. S., and Landry, H.: A comparative performance evaluation of the AURAMS and CMAQ air quality modelling systems, Atmos. Environ., 43, 1059–1070, 2009.
Stroud, C. A., Morneau, G., Makar, P. A., Moran, M. D., Gong, W., Pabla, B., Zhang, J., et al.: OH-reactivity of volatile organic compounds at urban and rural sites across canada: Evaluation of air quality model predictions using speciated VOC measurements, Atmos. Environ. 42(33), 7746–7756, 2008.
Stull, R. B.: An Introduction to Boundary Layer Meteorology, Kluwer Academic Publishers, Boston, 666 pp., 1988.
Yap, D., Ning, D. T., and Dong, W.: An assessment of source contributions to the ozone concentrations in southern Ontario, 1979–1985, Atmos. Environ., 22, 1161–1168, 1988.

ACPD
10, 14241–14312, 2010

Table 1. Evaluation statistics for 3 June 2007–31 August 2007, 42-km and 15-km AURAMS versus AIRNow. M_obs = observed mean, M_mod = model mean, MB = mean bias, NMB = normalized mean bias, R = correlation coefficient, RMSE = root mean square error.

	O_3 daily 1-h max				O_3 daily mean				Hourly O_3			
	42-km	15-km	42-km east	15-km "BAQS Met"	42-km	15-km	42-km east	15-km "BAQS-Met"	42-km	15-km	42-km east"BAQS-Met"	15-km
Number of sites	1167	681	833	61	1167	681	833	61	1167	681	833	61
M_obs (ppbv)	56.9	57.7	55.6	57.9	32.6	33.3	31.7	33.6	33.0	33.7	32.1	34.0
M_mod (ppbv)	65.2	63.5	64.0	63.6	43.6	40.0	42.9	40.0	43.8	40.3	43.1	40.2
MB (ppbv)	8.4	5.8	8.4	5.7	11.0	6.7	11.3	6.5	10.8	6.5	11.0	6.2
NMB	0.16	0.10	0.16	0.10	0.38	0.22	0.37	0.21	0.37	0.21	0.36	0.19
R	0.46	0.44	0.49	0.44	0.43	0.39	0.46	0.33	0.60	0.61	0.63	0.61
RMSE (ppbv)	19.3	18.2	18.3	18.1	16.0	13.2	15.3	14.1	20.5	18.5	19.7	18.5

Note: "42-km east" denotes statistics computed for sites east of 100 W within the continental 42-km domain; "BAQS-Met" denotes statistics computed for sites within an area bound by 40.5–44.5 N and 84–78 W. Number of stations: 42-km: 1167, 42-km east: 833, 15-km: 681, 15-km "BAQS-Met": region bounded by 40.5 to 44.5 N and 78 to 84 W.

ACPD
10, 14241–14312, 2010

Table 2. zone statistics at all BAQS-Met surface mesonet stations, 2.5-km resolution simulations.

Statistic	O_3 hourly averages	O_3 daily mean	O_3 daily 1-h max	O_3 daily 1-h min
M_obs (ppbv)	41.2	41.8	63.2	21.5
M_mod (ppbv)	37.4	38.1	61.2	18.7
MB	−3.77	−3.78	−1.93	−2.83
NMB	−0.092	−0.090	−0.031	−0.132
R	0.63	0.60	0.57	0.60
RMSE (ppbv)	17.6	13.2	17.9	13.2

ACPD
10, 14241–14312, 2010

Table 3. Statistical comparison between 2.5 km AURAMS simulation and aircraft ozone observations.

Flight Number	*R*	Slope	Intercept	Mean Bias	Normalized Mean Bias	Mean Error	Normalized Mean Error	Number of Points
All Flights	7.40E-01	9.834E-01	−7.42E+00	−8.42E+00	−1.39E+01	1.23E+01	2.04E+01	939
1 (06/23 12:54–15:00)	6.65E-01	9.82E-01	−1.21E+01	−1.27E+01	−3.94E+01	1.27E+01	3.84E+01	56
2 (06/23 17:22–19:56)	2.83E-01	4.17E-01	1.18E+01	−1.15E+01	−2.87E+01	1.15E+01	2.89E+01	70
3 (06/23 21:34–22:16)	2.85E-01	2.76E-01	1.42E+01	−1.49E+01	−3.70E+01	1.49E+01	3.70E+01	15
4 (06/25 14:38–17:24)	5.39E-01	9.81E-01	−1.08E+01	−1.20E+01	−1.85E+01	1.26E+01	1.95E+01	67
5 (06/25 19:30–21:54)	5.27E-01	5.86E-01	1.81E+01	−1.20E+01	−1.65E+01	1.39E+01	1.91E+01	68
6 (06/25 23:00–06/26 0:00)	−2.03E-02	−2.02E-02	6.21E+01	−1.16E+01	−1.60E+01	1.18E+01	1.63E+01	23
7 (06/26 12:34–15:06)	−2.10E-01	−1.78E-01	7.71E+01	−3.12E+00	−4.59E+00	7.55E+00	1.11E+01	67
8 (06/26 17:20–19:04)	4.01E-01	2.73E-01	4.87E+01	−3.01E+00	−4.23E+00	5.87E+00	8.25E+00	48
9 (06/26 20:10–22:20)	4.10E-01	5.77E-01	2.67E+01	−3.01E+00	−4.28E+00	9.13E+00	1.30E+01	61
10 (06/27 12:30–13:42)	4.78E-01	1.00E+00	−6.33E-02	−5.27E-02	−1.20E-01	6.38E+00	1.46E+01	28
11 (06/27 15:10–17:40)	6.22E-01	5.64E-01	3.37E+01	6.45E+00	1.03E+01	9.19E+00	1.47E+01	64
12 (07/03 22:44–07/04 13:00)	3.84E-01	4.32E-01	1.24E+01	−2.50E+01	−3.79E+01	2.50E+01	3.80E+01	71
13 (07/07 08:18–11:16)	3.66E-01	2.00E-01	1.85E+01	−1.78E+01	−3.92E+01	1.83E+01	4.02E+01	77
14 (07/07 17:30–20:20)	−4.27E-02	−5.51E-02	4.99E+01	−1.72E+01	−2.70E+01	1.86E+01	2.92E+01	75
15 (07/08 15:20–18:12)	7.33E-01	1.37E+00	−2.07E+01	4.09E+00	6.17E+00	8.59E+00	1.29E+01	76
16 (07/08 22:20–07/09 1:00)	3.97E-01	7.82E-01	1.48E+01	−4.81E-01	−6.89E-01	6.08E+00	8.70E+00	73

ACPD
10, 14241–14312, 2010

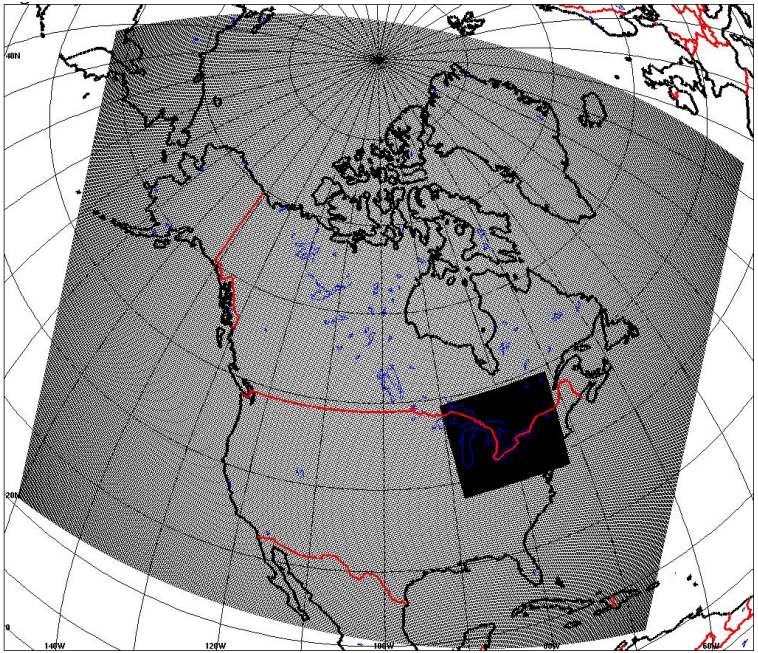

Fig. 1. GEM 15-km and 2.5-km domains.

ACPD
10, 14241–14312, 2010

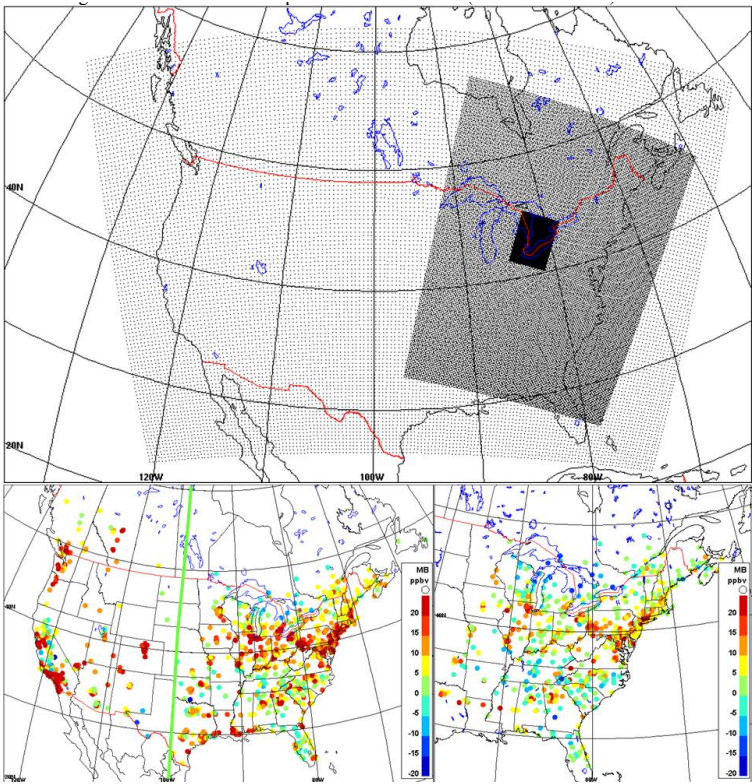

Fig. 2. **(a)** AURAMS 42-km, 15-km, and 2.5-km domains, **(b)** monitoring stations used for 42 km comparison to observations (Mean Bias shown; region east of 100 W is "42-km-East"); **(c)** monitoring sites used for 15-km comparison to observations (Mean Bias shown).

ACPD
10, 14241–14312, 2010

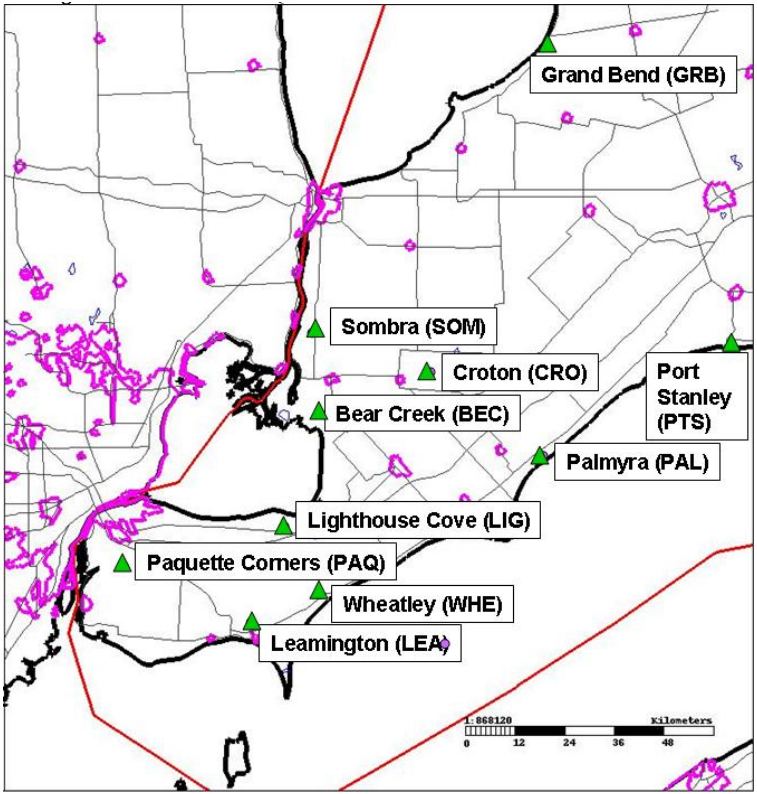

Fig. 3. Locations of BAQS-Met surface mesonet stations.

ACPD
10, 14241–14312, 2010

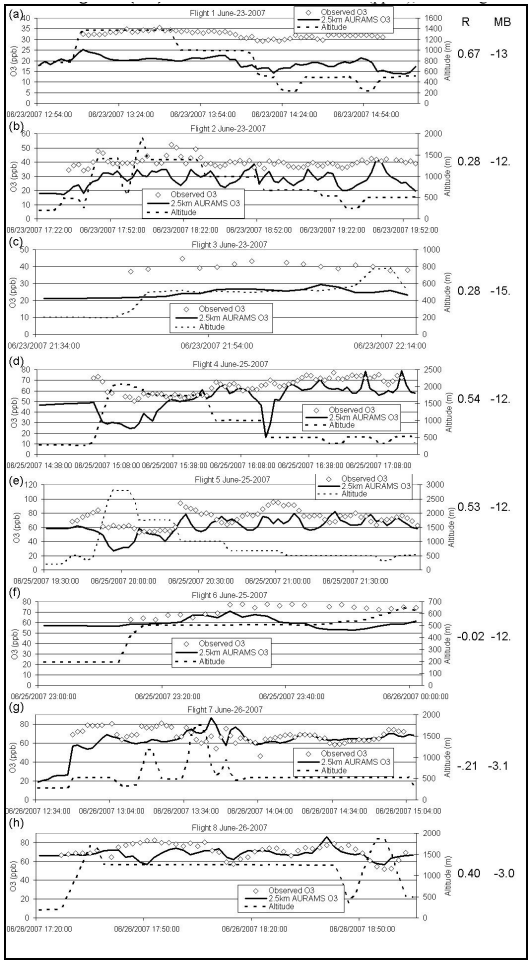

Fig. 4. Observed and simulated O_3 (ppbv).

ACPD
10, 14241–14312, 2010

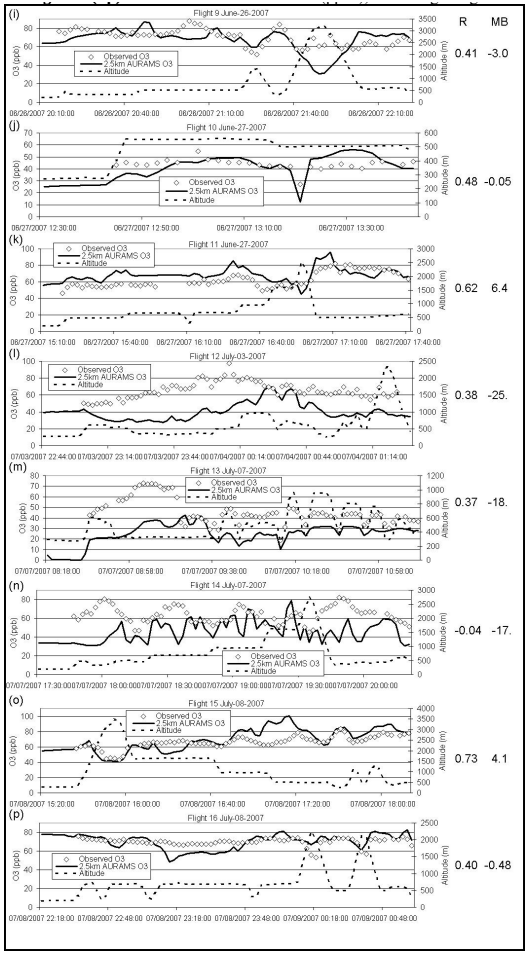

Fig. 4. Continued.

ACPD
10, 14241–14312, 2010

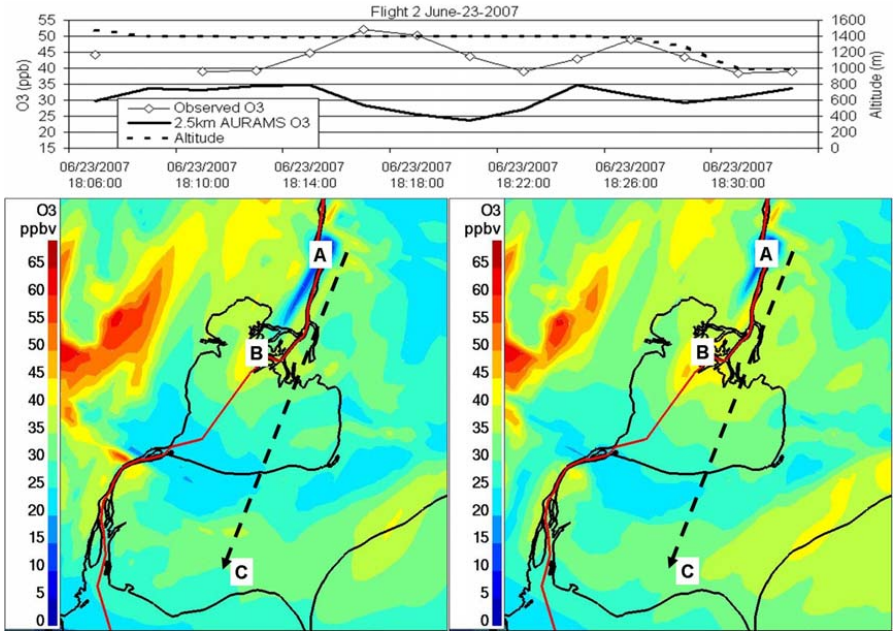

Fig. 5. (a) Comparison of observed and model ozone, 18:06 to 18:32 UT, 23 June. **(b)** Model-predicted ozone field at 1235 m a.g.l. (~1435 m a.s.l.), 18:20 UT, 23 June 2007, **(c)** same as (b), at 1500 m a.g.l. (~1700 m a.s.l.).

ACPD
10, 14241–14312, 2010

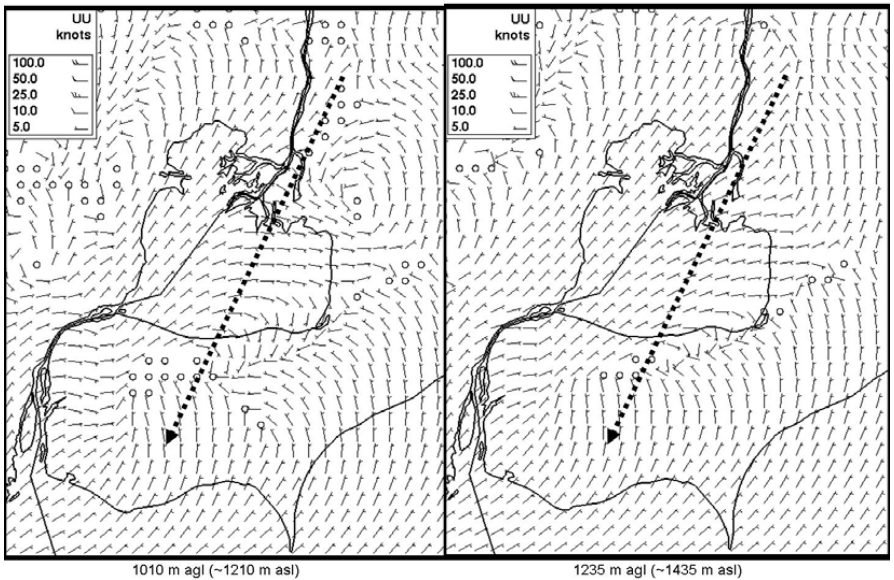

Fig. 6. **(a)** Model-predicted winds at 1010 m a.g.l. (~1210 m a.s.l.), **(b)** model-predicted winds at 1235 m a.g.l. (~1435 m a.s.l.).

ACPD
10, 14241–14312, 2010

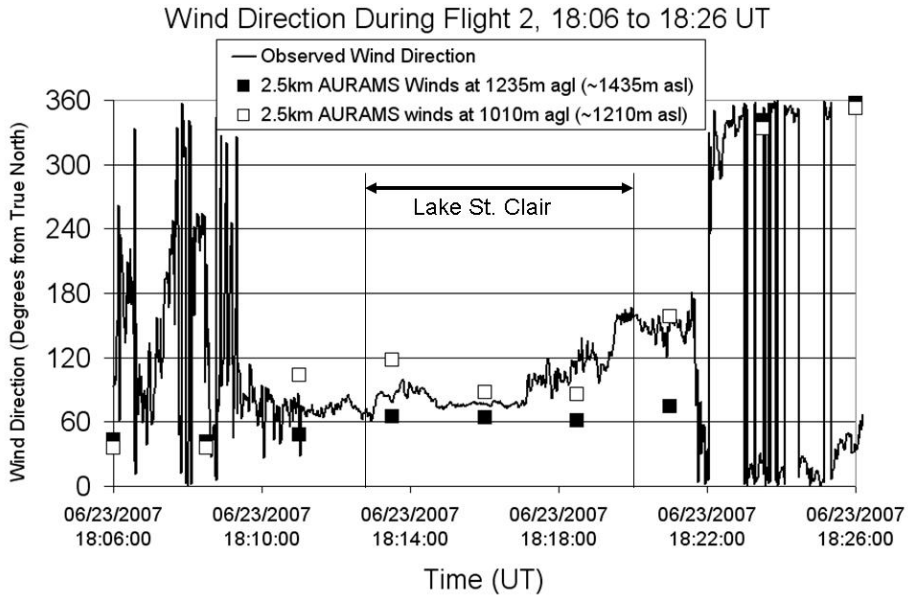

Fig. 7. Comparison of model and observed winds along this section of the flight path, 18:00 model output.

ACPD
10, 14241–14312, 2010

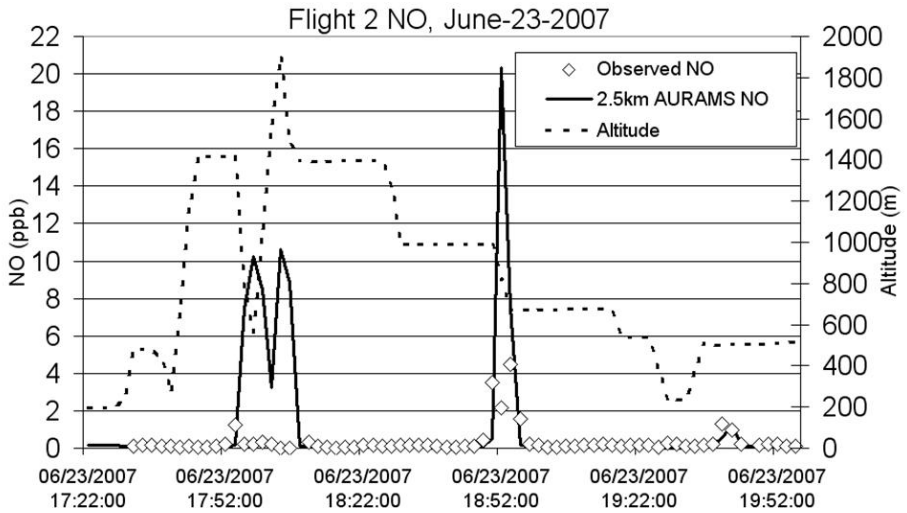

Fig. 8. Comparison of observed and modelled NO, flight 2 (ppbv).

ACPD
10, 14241–14312, 2010

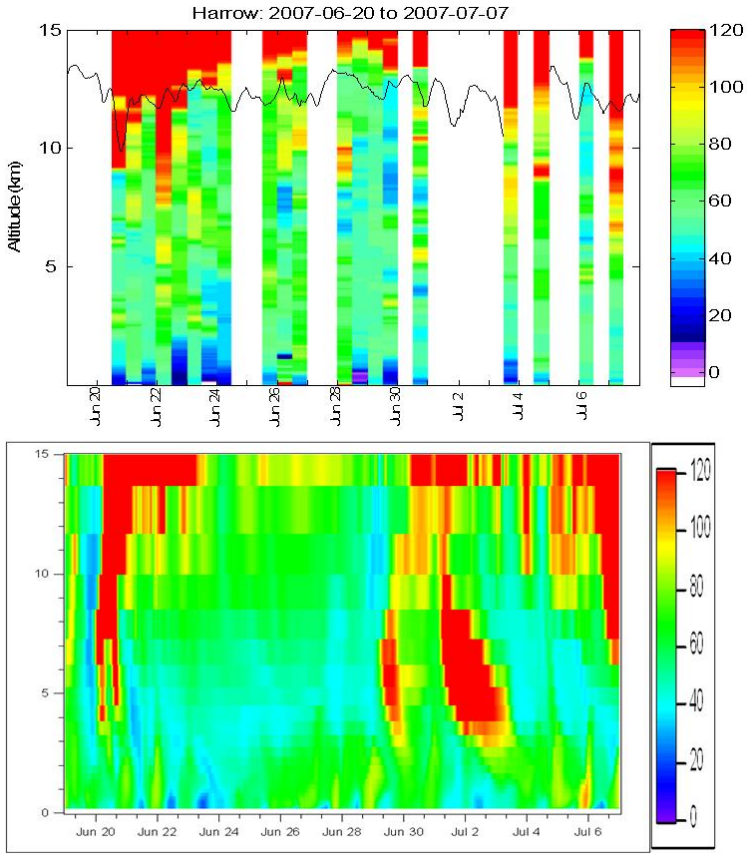

Fig. 9. (a) Observed ozone profiles from sondes, **(b)** Model-simulated ozone profiles.

ACPD
10, 14241–14312, 2010

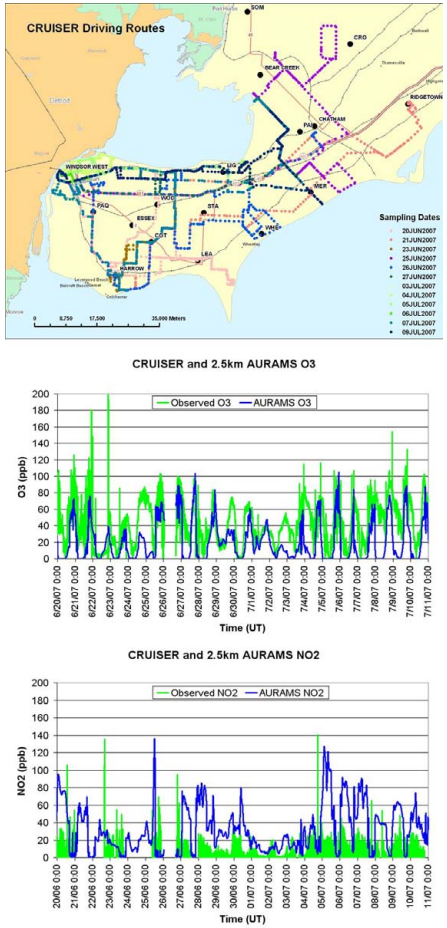

Fig. 10. **(a)** CRUISER driving routes during the intensive, **(b)** observed and model-simulated ozone along CRUISER driving routes, **(c)** observed and simulated NO_2 along CRUISER driving routes.

ACPD
10, 14241–14312, 2010

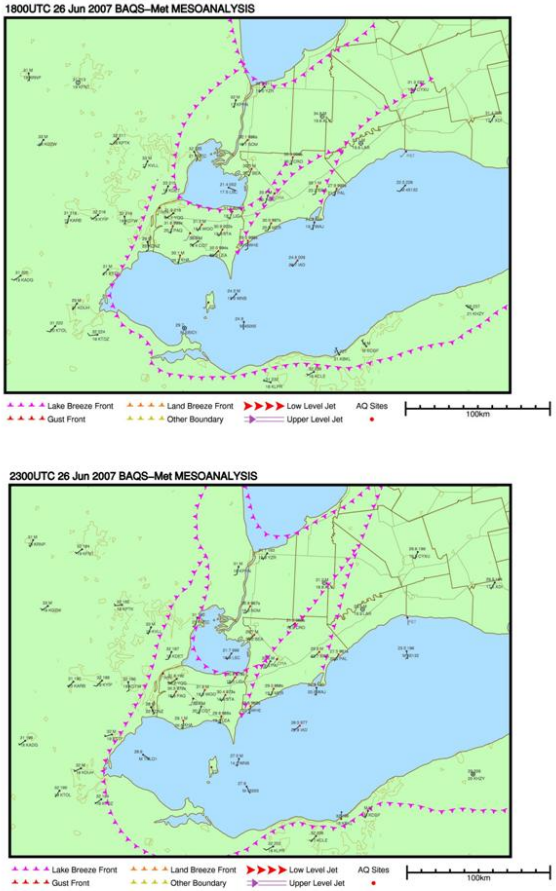

Fig. 11. Meso-analysis lake-breeze front locations on 26 June at **(a)** 18:00 UT (02:00 p.m. local time), **(b)** 23:00 UT (07:00 p.m. local time).

ACPD
10, 14241–14312, 2010

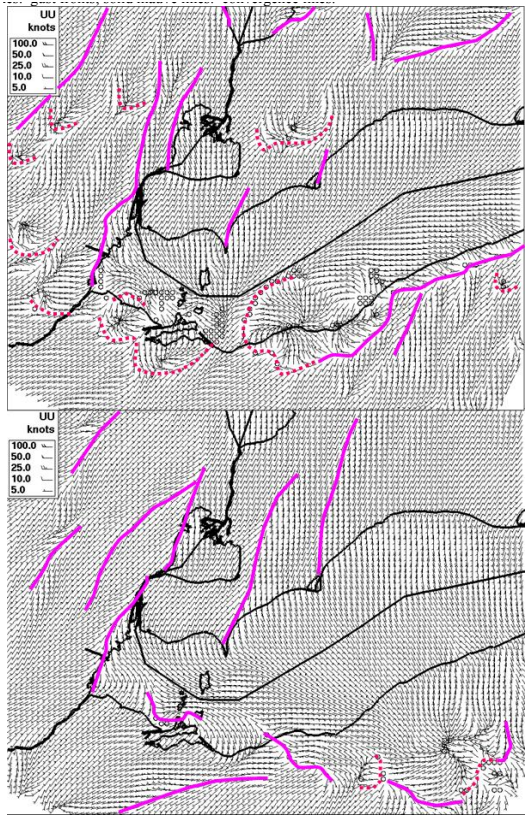

Fig. 12. Lake-breeze front locations inferred from convergence pattern of 2.5-km resolution model winds on 26 June at **(b)** 18:00 UT (02:00 p.m. local time), **(b)** 23:00 UT (07:00 p.m. local time). Dashed red lines: gust fronts; solid mauve lines: convergence lines.

ACPD
10, 14241–14312, 2010

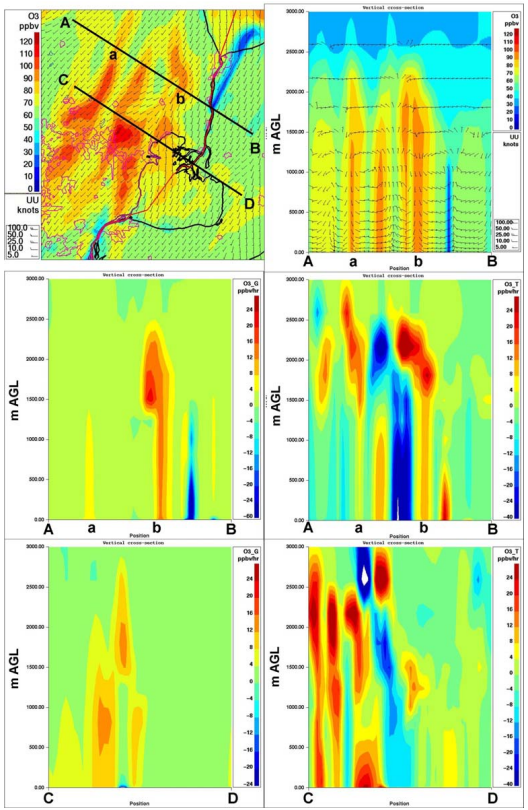

Fig. 13. Model-predicted fields for 26 June 18:00 UT (02:00 p.m. local time). **(a)** Surface ozone and wind barbs; **(b)** Vertical profile of ozone and winds along cross-section A–B of (14a); **(c)** As in (b) but gas-phase photochemical production; **(d)** As in (b) but total transport rate of change of ozone along cross-section A–B; **(e)** Gas-phase photochemical production and loss along cross-section C–D; **(f)** Total transport rate of change along cross-section C–D.

ACPD
10, 14241–14312, 2010

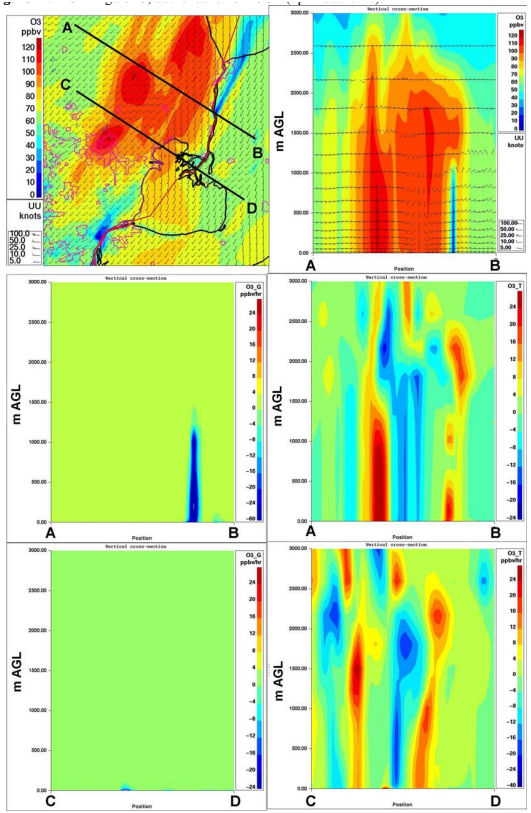

Fig. 14. As in Fig. 13, but for 26 June 23:00 UT (07:00 p.m. local time).

ACPD
10, 14241–14312, 2010

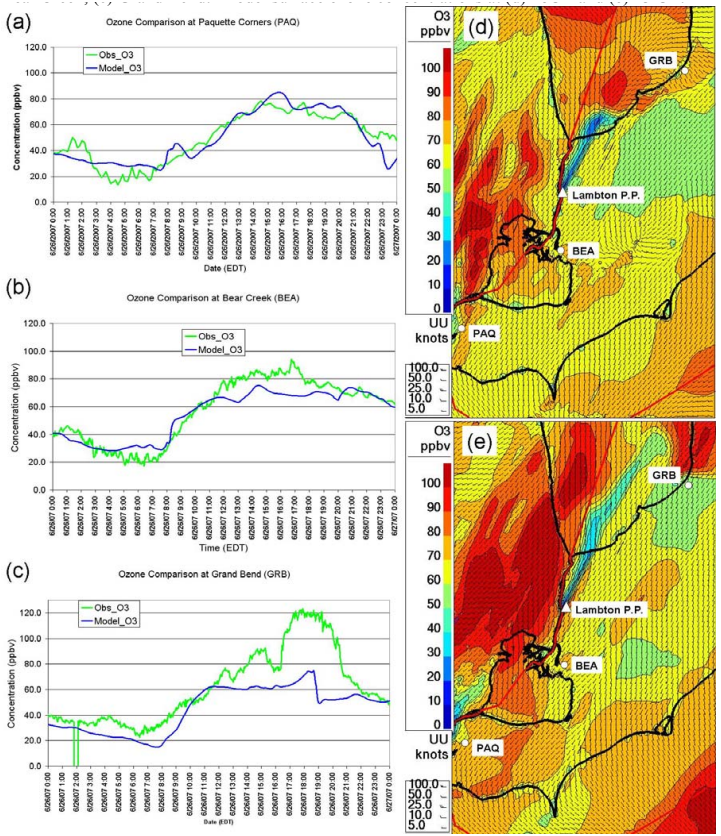

Fig. 15. Ozone comparison with surface observations, 26 June, at **(a)** Paquette Corners, **(b)** Bear Creek, **(c)** Grand Bend. Model surface ozone concentrations at **(d)** 18:00 UT and **(e)** 23:00 UT.

ACPD
10, 14241–14312, 2010

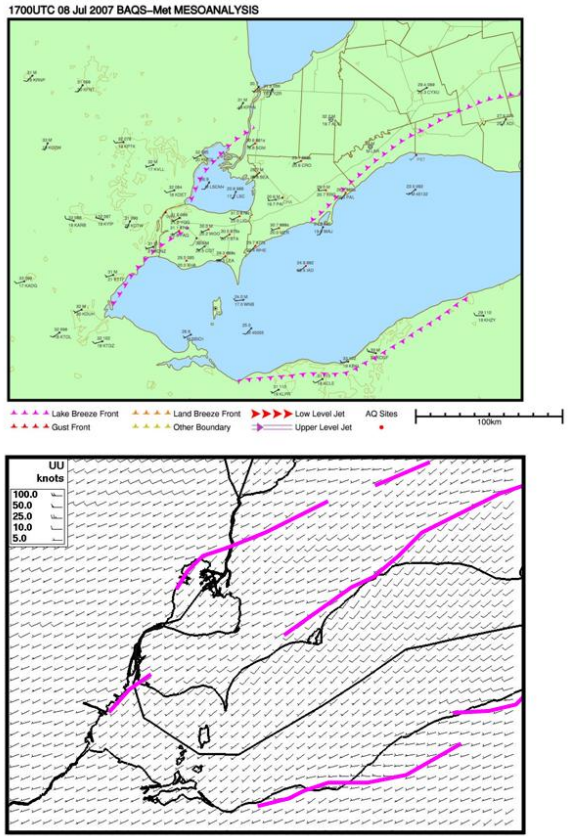

Fig. 16. **(a)** Meso-analysis lake-breeze front locations on 8 July, 17:00 UT (01:00 p.m. local time); **(b)** Model-predicted surface wind field and convergence zones.

ACPD
10, 14241–14312, 2010

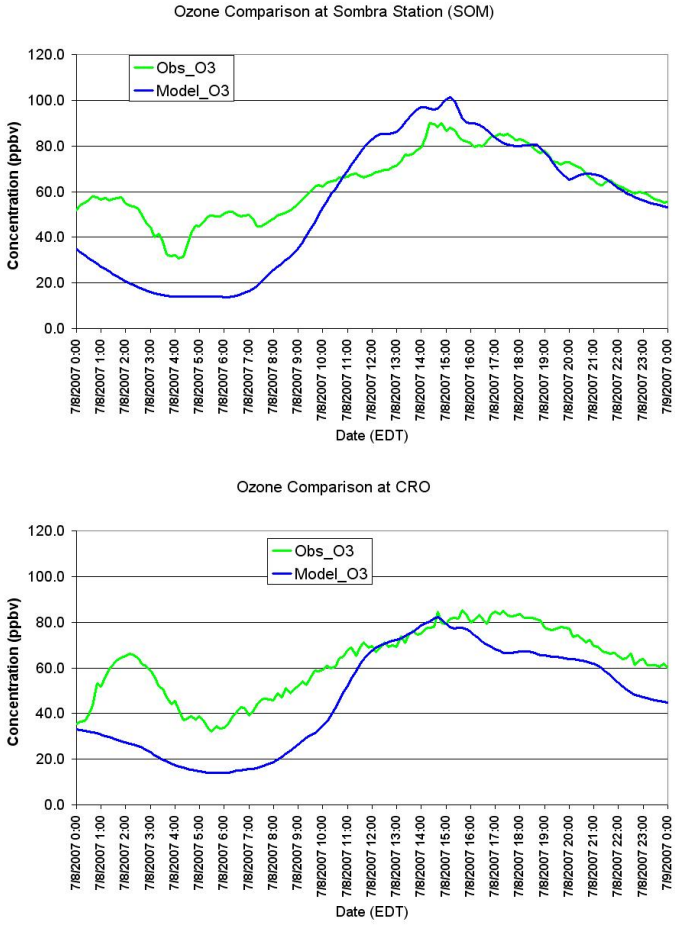

Fig. 17. Model-predicted ozone versus observations, 8 July. **(a)** Sombra, **(b)** Croton.

ACPD
10, 14241–14312, 2010

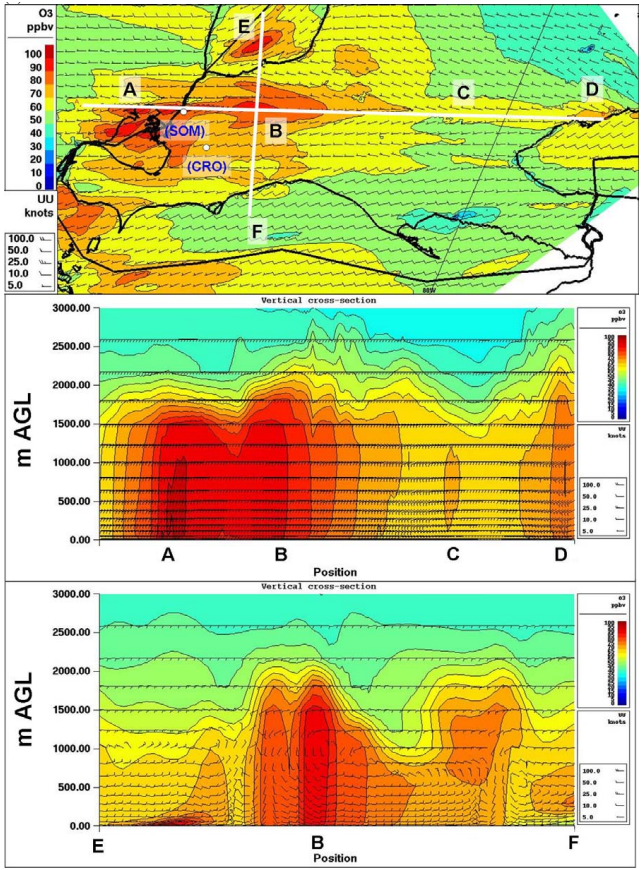

Fig. 18. Model-predicted ozone and wind fields on 8 July, 17:00 UT (01:00 p.m. local time); **(a)** surface concentrations and wind fields; **(b)** vertical cross-section from North Detroit to Toronto, **(c)** vertical cross-section from Lake Huron to Lake Erie.

ACPD
10, 14241–14312, 2010

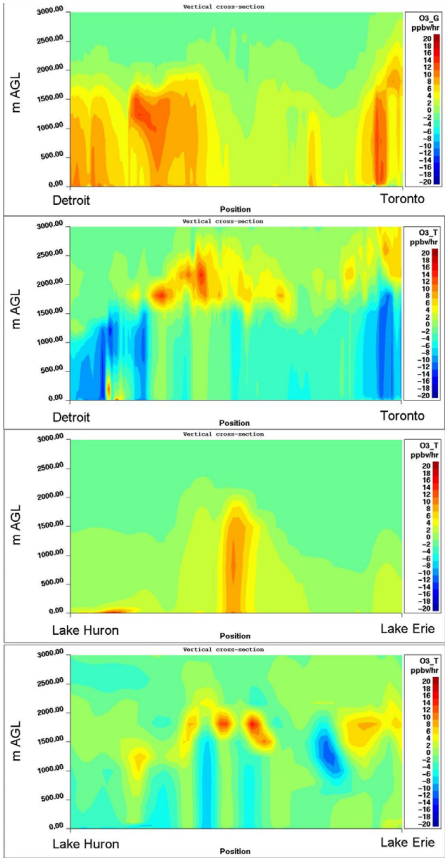

Fig. 19. Model-predicted fields for 8 July, 17:00 UT (01:00 p.m. local time). **(a)** Gas-phase photochemical production, Detroit to Toronto cross-section; **(b)** total transport rate of change, Detroit to Toronto cross-section; **(c)** gas-phase photochemical production, Lake Huron to Lake Erie cross-section; **(d)** total transport rate of change, Lake Huron to Lake Erie cross-section.

ACPD
10, 14241–14312, 2010

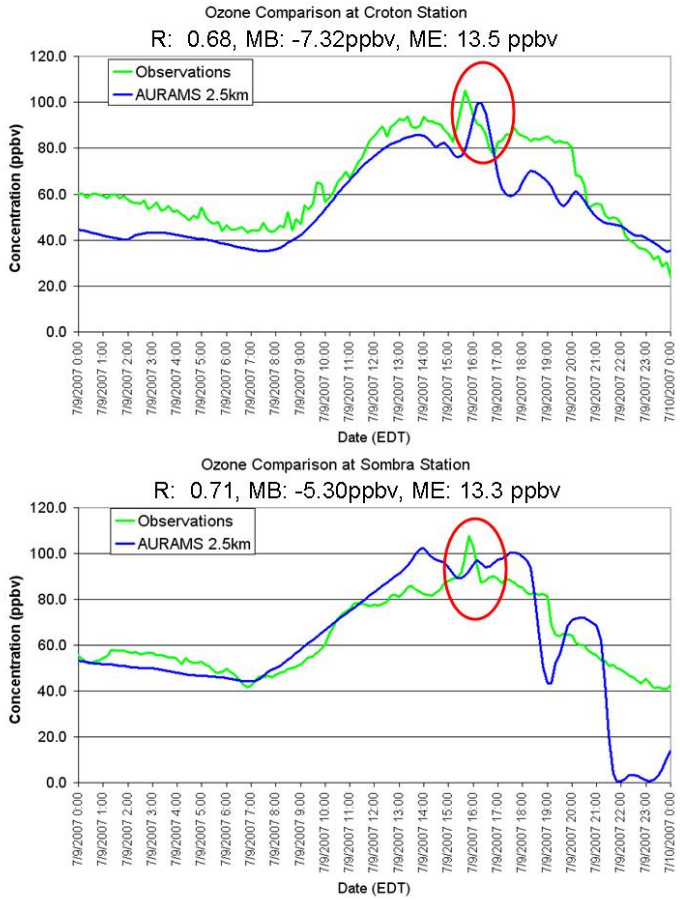

Fig. 20. Model-predicted surface ozone and wind fields for 9 July at **(a)** Croton, **(b)** Sombra. Circled region identifies observed spike in local ozone concentrations, likely associated with ozone created over Lake St. Clair. Statistical measures are for the entire measurement intensive.

ACPD
10, 14241–14312, 2010

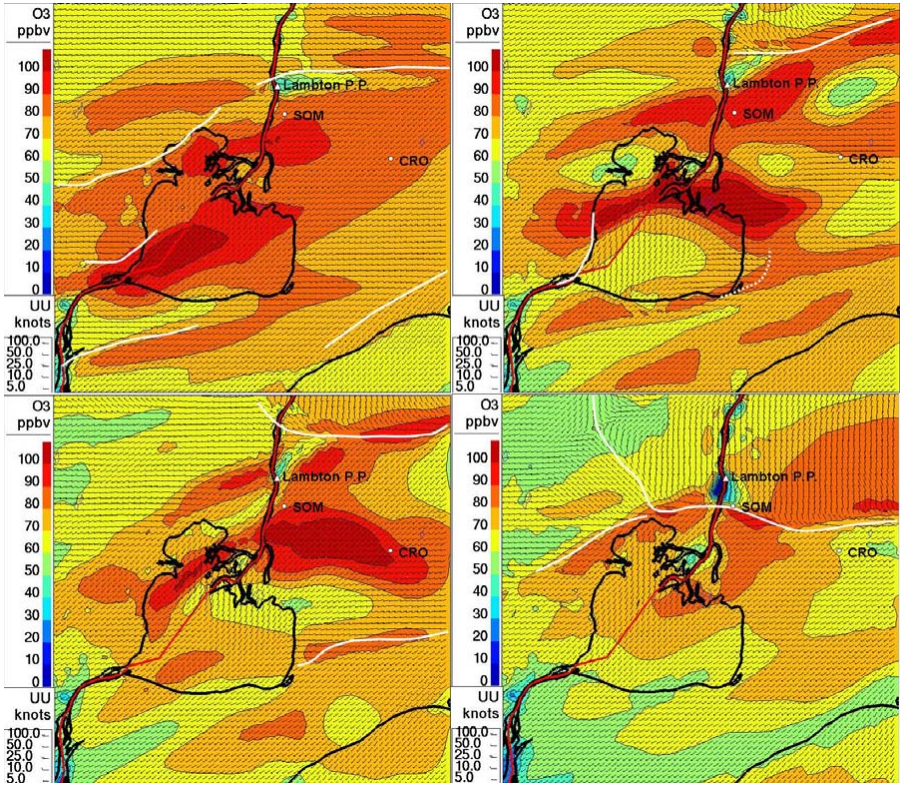

Fig. 21. Model-predicted surface ozone and wind fields for 9 July, **(a)** 17:00 UT (01:00 pm local time); **(b)** 19:00 UT (03:00 p.m.); **(c)** 20:00 UT (04:00 p.m.); **(d)** 22:00 UT (06:00 p.m.). SOM: Sombra station. CRO: Croton station. Lambton P.P. = Lambton Power-Plant.

ACPD
10, 14241–14312, 2010

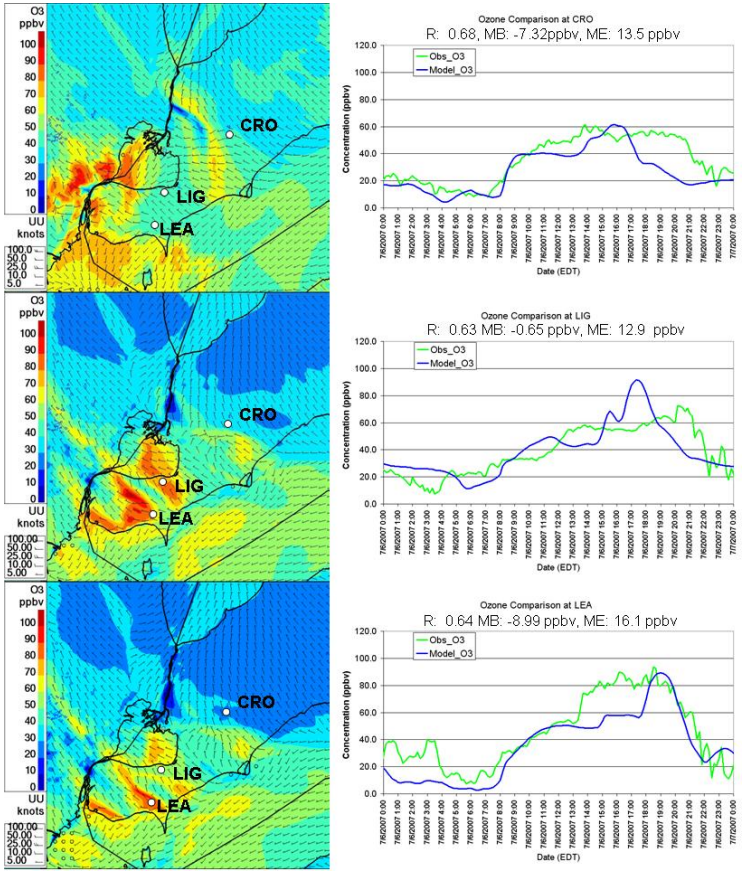

Fig. 22. Surface station analysis at Croton (CRO), Lighthouse cove (LIG) and Leamington stations, 6 July. **(a)**, **(c)**, **(e)**: model-generated surface ozone and wind fields at 18:00, 22:00, 23:00 UT (14:00, 18:00, 19:00 EDT). **(b)**, **(d)**, **(f)**: model and observed ozone time series at CRO, LIG and PAL stations.

ACPD
10, 14241–14312, 2010

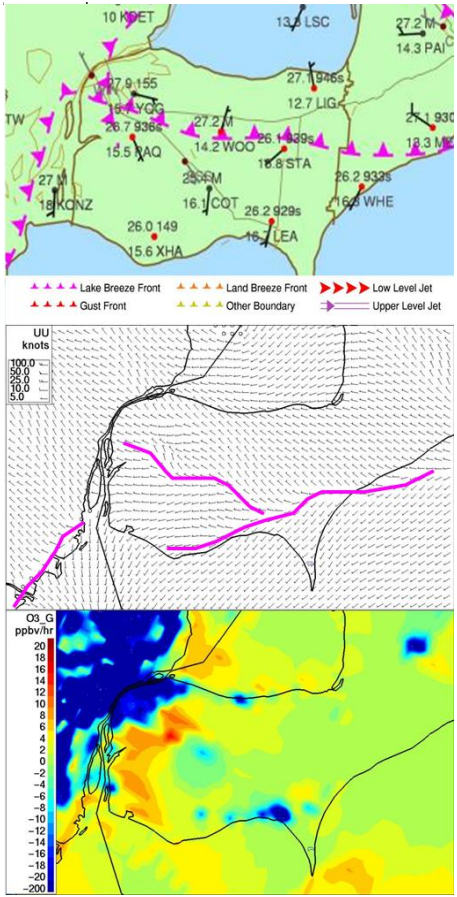

Fig. 23. 6 July 20:00 UT **(a)** Mesoanalysis, **(b)** Model-predicted wind fields and surface convergence areas (with direction of winds at met stations as large arrows for clarity), **(c)** model-predicted gas-phase ozone production and loss.

ACPD
10, 14241–14312, 2010

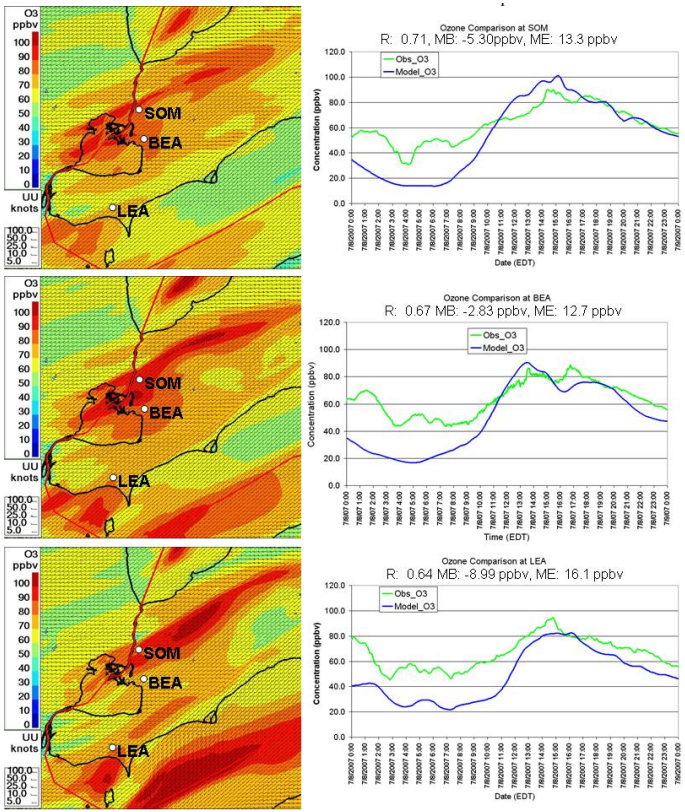

Fig. 24. Surface station analysis at Sombra (SOM), Bear Creek (BEA) and Leamington (LEA) stations, 8 July. **(a)**, **(c)**, **(e)**: model-generated surface ozone and wind fields at 17:00, 18:00, 20:00 UT (13:00, 14:00, 16:00 EDT). **(b)**, **(d)**, **(f)**: model and observed ozone time series at SOM, BEA and LEA stations. Statistical measures are for the entire measurement intensive period.

ACPD
10, 14241–14312, 2010

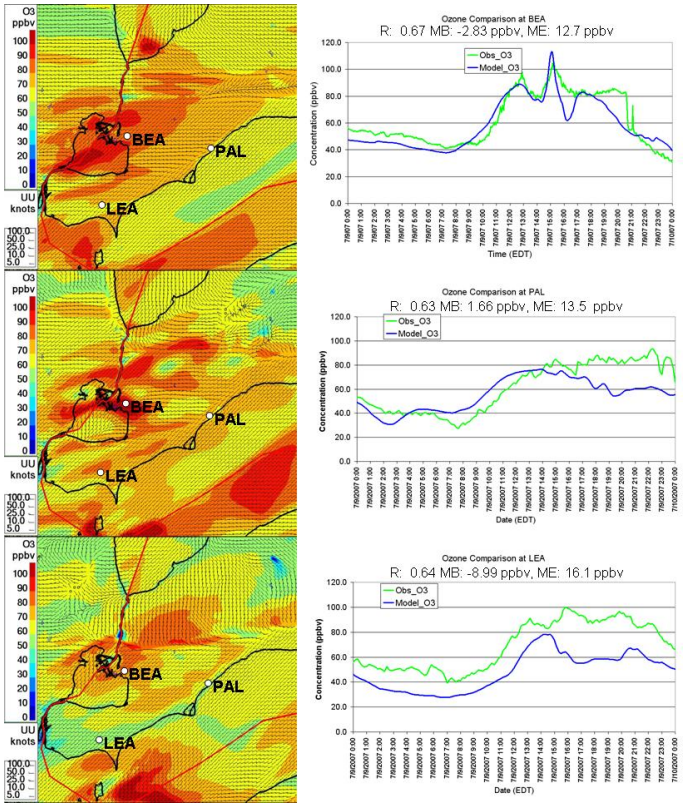

Fig. 25. Surface station analysis at Bear Creek (BEA), Palymyra (PAL) and Leamington (LEA) stations, 9 July. **(a)**, **(c)**, **(e)**: model-generated surface ozone and wind fields at 17:00, 19:00, 22:00 UT (13:00, 15:00, 18:00 EDT). **(b)**, **(d)**, **(f)**: model and observed ozone time series at BEA, PAL, and LEA stations.

ACPD
10, 14241–14312, 2010

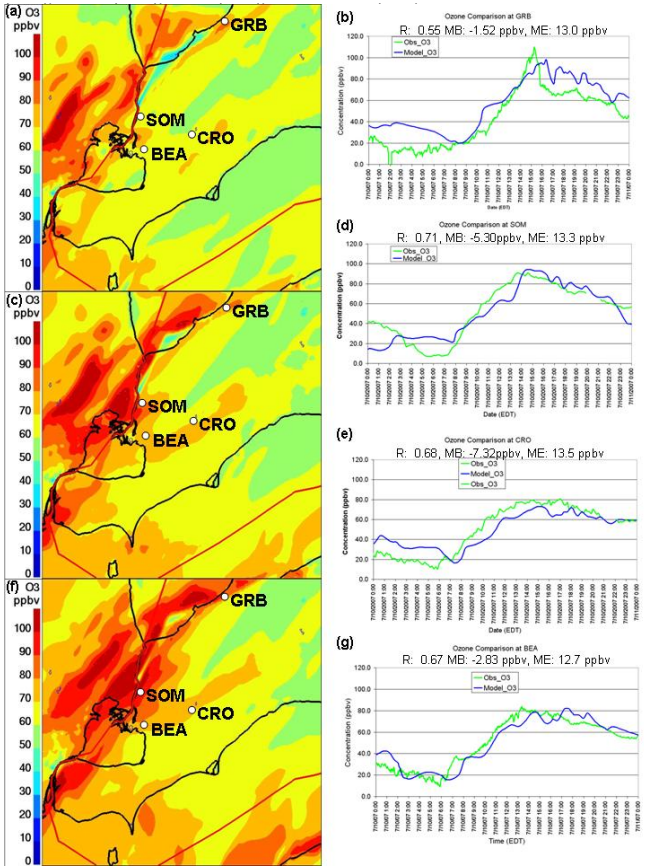

Fig. 26. Surface station analysis at Grand Bend (GRB), Sombra (SOM), Croton (CRO) and Bear Creek (BEA) stations, 10 July. **(a)**, **(c)**, **(f)**: model-generated surface ozone at 17:00, 18:00, 19:00 UT (13:00, 14:00, 15:00 EDT). **(b)**, **(d)**, **(e)**, **(g)**: model and observed ozone time series at Grand Bend (GRB), Sombra (SOM), Croton (CRO), and Bear Creek (BEA) stations.

ACPD
10, 14241–14312, 2010

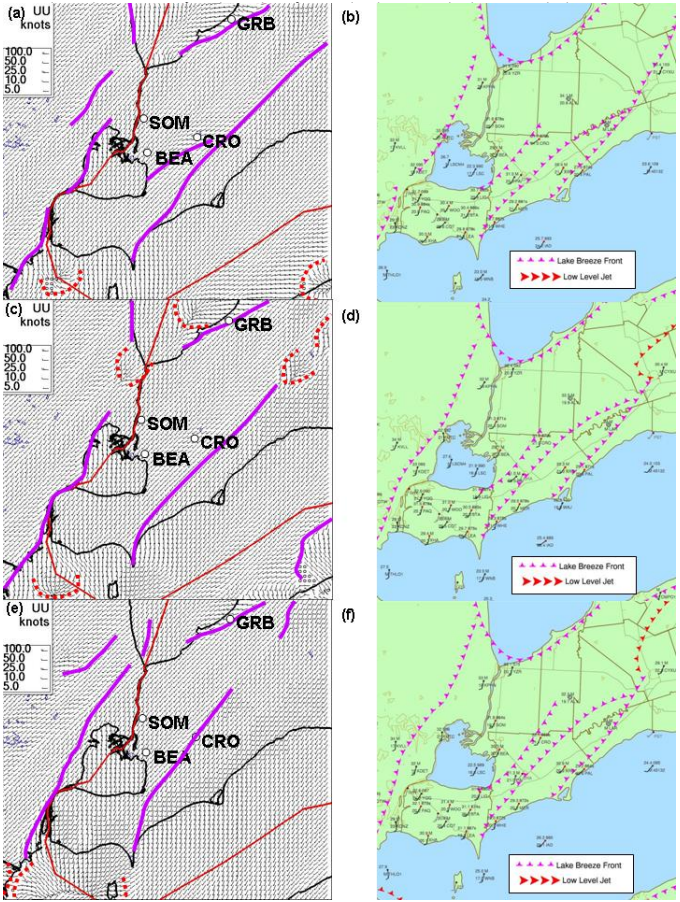

Fig. 27. Comparison between model-generated surface winds, convergence lines, and gust fronts **(a, c, e)** to mesoanalysis **(b, d, f)**, 10 July. (a, b): 17:00 UT. (c, d): 18:00 UT. (e,f): 19:00 UT.

ACPD
10, 14241–14312, 2010

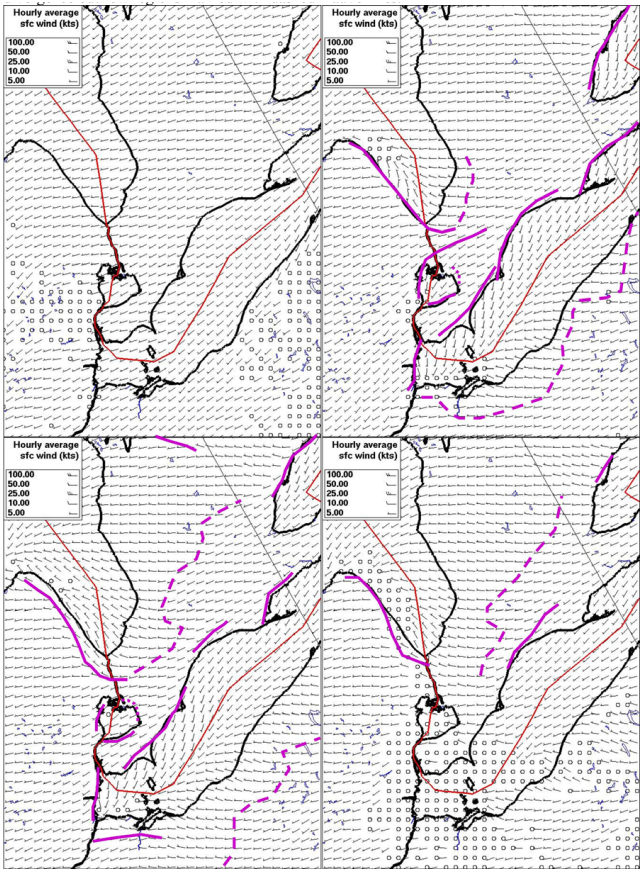

Fig. 28. 23 day average wind fields at **(a)** 12:00 UT, **(b)** 16:00 UT, **(c)** 20:00 UT, and **(d)** 00:00 UT; 08:00 a.m., 12:00 p.m., 04:00 p.m. and 08:00 p.m., respectively. Convergence regions marked as solid mauve lines, boundary of divergence outflow regions marked with dashed mauve lines.

ACPD
10, 14241–14312, 2010

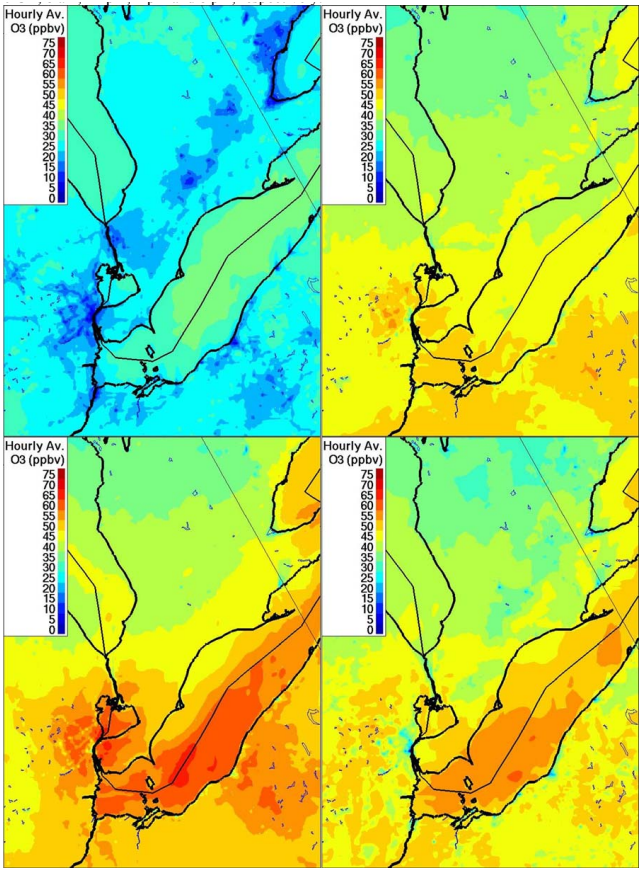

Fig. 29. 23 day average ozone concentration fields at **(a)** 12:00 UT, **(b)** 16:00 UT, **(c)** 20:00 UT, and **(d)** 00:00 UT; 08:00 a.m., 12:00 p.m., 04:00 p.m. and 08:00 p.m., respectively.

ACPD
10, 14241–14312, 2010

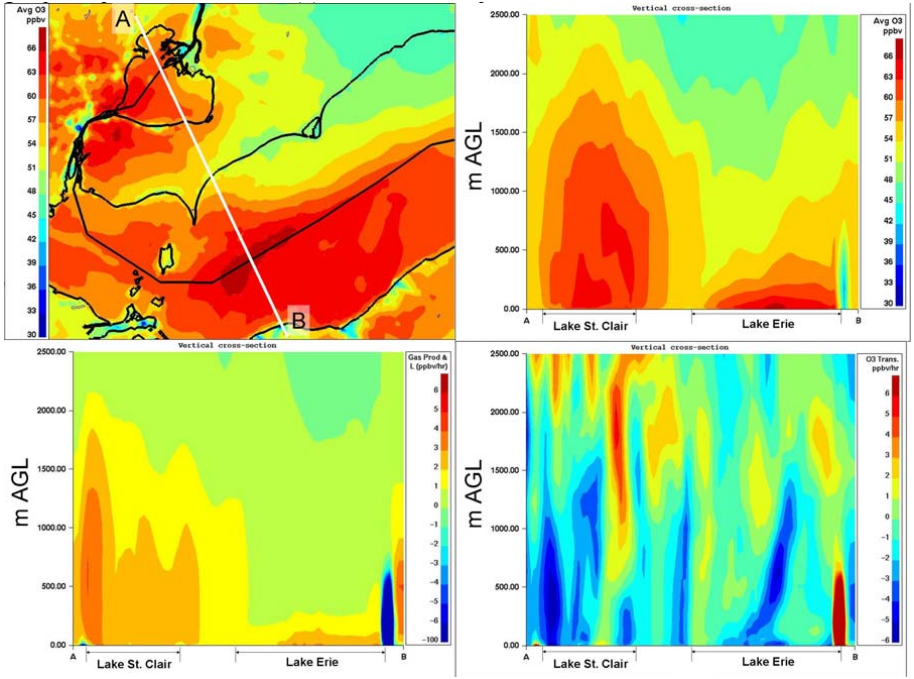

Fig. 30. 23 day average values at 20 Z (04:00 p.m. local time): **(a)** surface ozone over Lake St. Clair and Lake Erie, showing location of cross-section used for **(b)** ozone concentration, **(c)** ozone gas-phase production and loss, **(d)** ozone total transport.

ACPD
10, 14241–14312, 2010

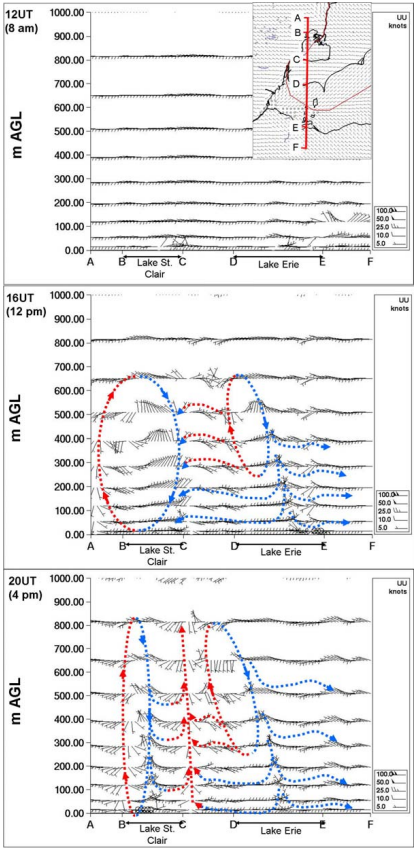

Fig. 31. Cross-section of 3-D wind fields across Lakes St. Clair and Erie at **(a)** 12:00 UT (08:00 a.m.), **(b)** 16:00 UT (12:00 noon), and **(c)** 20:00 UT (04:00 p.m.). Net upward motion streamlines are sketched in red, downward motion in blue. Inset: location of the cross-section, superimposed on 20:00 UT surface winds.

ACPD
10, 14241–14312, 2010